NIA Report No. 2007-08

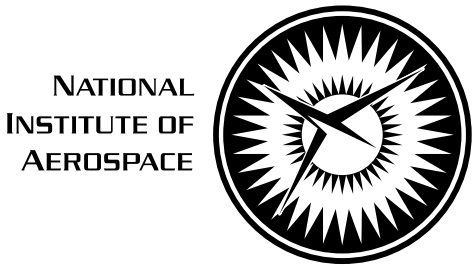

Accuracy Analysis for Mixed-Element Finite-Volume Discretization Schemes

Boris Diskin
National Institute of Aerospace, Hampton, Virginia

James L. Thomas
NASA Langley Research Center, Hampton, Virginia

August 2007

ACCURACY ANALYSIS FOR MIXED-ELEMENT FINITE-VOLUME DISCRETIZATION SCHEMES

Boris Diskin* and James L. Thomas†

ABSTRACT

A new computational analysis tool, downscaling (DS) test, has been introduced and applied for studying the convergence rates of truncation and discretization errors of finite-volume discretization (FVD) schemes on general unstructured grids. The study corrects a misconception that the discretization accuracy of FVD schemes on irregular grids is directly linked to convergence of truncation errors. The DS test is a general, efficient, accurate, and practical tool, enabling straightforward extension of verification and validation to general unstructured grid formulations. It also allows separate analysis of the interior, boundaries, and singularities that could be useful even in structured-grid settings. There are several new findings arising from the use of the DS test analysis. It was shown that the discretization accuracy of a common node-centered FVD scheme, known to be second-order accurate for inviscid equations on triangular grids, degenerates to first order for certain mixed-element grids. Alternative node-centered schemes have been presented and demonstrated to provide second and third order accuracies on general mixed-element grids. The local accuracy deterioration at intersections of tangency and inflow/outflow boundaries has been demonstrated using the DS tests tailored to examining the local behavior of the boundary conditions. The discretization-error order reduction within inviscid stagnation regions has been demonstrated. The accuracy deterioration is local, affecting mainly the velocity components, but applies to any order scheme.

1 INTRODUCTION

There is an increasing reliance on computational simulations in aircraft design practices, supplementing traditional analytic and experimental approaches. Verification and validation methodologies [15] are being developed to ensure the correct applicability of these approaches in practical applications. Verification methodologies for structured grids, e.g., [12], are relatively well-developed in comparison to unstructured grids, especially grids containing mixed elements or grids derived through agglomeration techniques. The summary of the latest of three Drag Prediction Workshops [9] illustrates the problems associated with assessing errors in practical complex-geometry/complex-physics applications.

Finite-volume discretization (FVD) methods are widely used in computations on unstructured grids. However, the methods for analyzing accuracy of FVD schemes on practical grids are not well established. Issues related to accuracy of unstructured FVD methods have recently been addressed in several publications [11, 13, 14]. In this paper, we introduce a practical method for evaluating the accuracy of finite-volume discretization (FVD) schemes defined on general unstructured meshes.

*National Institute of Aerospace (NIA), 100 Exploration Way, Hampton, VA 23666 (bdiskin@nianet.org). This research was supported by the National Institute of Aerospace under NASA Task NNL07AA23C

†Computational Aerosciences Branch, NASA Langley Research Center, Mail Stop 128, Hampton, VA 23681-2199 (James.L.Thomas@nasa.gov).

In a two-dimensional (2D) domain, the considered primal meshes are composed of triangular and quadrilateral cells. The FVD schemes are derived from the integral form of a conservation law

$$\oint_{\Gamma} (\mathbf{F} \cdot \hat{\mathbf{n}}) \, d\Gamma = \iint_{\Omega} (f - S) \, d\Omega, \tag{1}$$

where f is a forcing function independent of the solution, S is a solution-dependent source function, Ω is a control volume with boundary Γ, $\hat{\mathbf{n}}$ is the outward unit normal vector, and $\mathbf{F}$ is the flux vector. The general FVD approach requires partitioning the domain into a set of non-overlapping control volumes and implementing numerically equation (1) over each control volume. The focus of this paper is node-centered FVD schemes, where solution values are stored at the mesh nodes; however, the proposed analysis techniques can be straightforwardly applied to cell-centered FVD schemes.

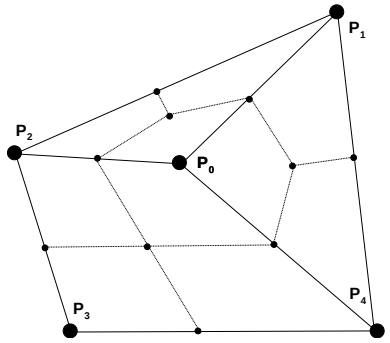

Figure 1: *Median-dual partition for node-centered finite-volume discretizations.* $P_0 - P_4$ *denote grid nodes.*

For 2D node-centered FVD schemes, a *median-dual* partition can be constructed by connecting the centriods of the primal-mesh cells with the midpoints of the surrounding edges (Figure 1). These non-overlapping control volumes cover the entire computational domain and compose a mesh that is dual to the primal mesh.

The discrete solution is represented as a piecewise polynomial function; the polynomials are defined within either primal or dual cells. The discretization is applied at a sequence of refined grids satisfying the *consistent refinement property*. The property requires the maximum distance across primal and dual cells to decrease consistently with increase of the total number of grid points, *N*. In particular, the maximum distance should tend to zero as $N^{-1/2}$ in 2D computations.

The main accuracy measure of any FVD scheme is the *discretization error*, E_d, defined as the difference between the exact continuous solution, Q, to the differential conservation law

$$\nabla \mathbf{F} = f - S \tag{2}$$

and the exact discrete solution, Q^h, of the discretized equations (1)

$$E_d = Q - Q^h. \tag{3}$$

A common approach to evaluate the accuracy of a FVD scheme is to monitor the convergence of *truncation errors*. Truncation error, E_t, measures the accuracy of the discrete approximation

to the differential equations (2) and is defined as the residual obtained after substituting the exact solution Q into the normalized discrete equations (1),

$$E_t = \frac{1}{|\Omega|}\left[\iint\limits_{\Omega}\left(f^h - S^h\left(Q\right)\right)\,d\Omega - \oint\limits_{\Gamma}\left(\mathbf{F^h}\left(Q\right)\cdot\hat{\mathbf{n}}\right)\,d\Gamma\right], \tag{4}$$

where $\mathbf{F^h}$ is a reconstruction of the flux $\mathbf{F}$ at the boundary Γ, $|\Omega|$ is the measure of the control volume,

$$|\Omega| = \iint\limits_{\Omega} d\Omega, \tag{5}$$

f^h and S^h are, respectively, approximations of the forcing function f and the source function S on Ω, and the integrals are computed according to some quadrature formulas. Convergence of truncation errors has been applied as a FVD accuracy measure on both structured (regular) and unstructured (irregular) grids [5, 17]. On structured grids, this approach is well justified, as the truncation error converges as $O(h^p)$ on sequences of consistently refined grids, where h is a characteristic meshsize and p is the design discretization-accuracy order of the method. However, the truncation-error convergence is often misleading for unstructured grids. Several studies, e.g., [11, 17], noted that 2^{nd}-order convergence of truncation errors for some commonly used node-centered FVD schemes can be achieved only on grids with a certain degree of geometric regularity. Examples in subsequent sections show that such degradation of truncation-error convergence does not necessarily imply a lower-order convergence of discretization errors; the design-order discretization-error convergence can be achieved even when truncation errors exhibit a lower-order convergence or, in some cases, do not converge at all.

Although the convergence of unstructured-grid truncation errors is not identical to the discretization-error convergence, it still can be monitored to indicate if the design order of the discretization accuracy can be achieved. On a sequence of truly unstructured grids satisfying the consistent refinement property, the convergence order of truncation errors is typically less than the discretization-error convergence order by 1 for inviscid equations and by 2 for viscous equations.

The main *computational* tool introduced in this paper for evaluating accuracy of discretization schemes is a *downscaling (DS) test*. Performed for a known exact or manufactured solution, the test consists of a series of inexpensive computational experiments that account for local properties of the studied scheme; it is designed to provide estimates for the convergence orders of the discretization and truncation errors by comparing errors obtained on different scales. The DS test is a very general technique that can be applied to arbitrary grids and geometries. It can be tailored to study the discretization accuracy in the interior, at the boundary, and/or in vicinity of singularities. Analysis methods predicting the performance of DS tests have also been developed; examples are shown in Sections 4 and 5. While the computations presented in this paper are one- and two-dimensional, the analysis techniques and conclusions are fully expendable and have already been successfully applied in the three dimensions.

The material in this paper is organized as follows. Section 2 describes the construction and application of DS tests for general FVD schemes on unstructured grids. Section 3 introduces analytical methods for predicting convergence of discretization and truncation errors in a DS test.

Section 4 includes one-dimensional examples providing insights into convergence of the discretization and truncation errors on irregular grids. Section 5 analyzes convergence for several sets of 2D equations and FVD schemes and corroborates the analysis with numerical tests performed on randomly-split triangular, randomly-perturbed quadrilateral, and random mixed-element grids. In addition, the effects of flow singularities are analyzed; one-order deterioration of the discretization accuracy is observed and explained for inviscid stagnation flows. The concluding Section 6 summarizes the demonstrated computational and analytical results and discusses computational issues related to implementation of the improved-accuracy FVD schemes. The paper has four appendixes: Appendix A shows the computational complexity of extending the improved-accuracy FVD schemes to three dimensions; Appendix B illustrates an accuracy degeneration occurring on mixed-element grids for a common FVD scheme, known to be 2^{nd}-order accurate on general triangular grids; Appendix C reports on studies of the discretization errors generated at non-smooth interfaces on mixed-element grids composed of triangular and rectangular cells. Appendix D investigates discrepancies between the computational results presented in this paper and the results reported in [11].

2 DOWNSCALING (DS) TEST

The purpose of the downscaling (DS) test is to predict the discretization and truncation-error convergence orders in computations performed on general unstructured mixed-element grids satisfying the consistent refinement property. To apply a DS test, one first chooses a (manufactured) solution defined on the given computational domain. The associated forcing functions are found by substituting this solution into the continuous governing equations and boundary conditions.

The DS test requires numerical computations on a sequence of contracted domains zooming toward a focal point within the original computational domain (Figure 2). The choice of the focal-point location can be varied to study a typical interior discretization, a boundary discretization, or a specific singularity. Because the number of points in the DS-test domains is held (approximately) fixed, one can study solutions on grids with characteristic meshsizes much smaller than those of practical computations with a globally-refined grid sequence.

There are at least two possible strategies for grid generation on these contracted domains: (1) The first strategy is termed "scaled grid"; with this strategy, the first (coarsest) computational domain is defined as a subdomain of the investigated global mesh containing the focal point; other (finer) domains and their mesh patterns are derived by scaling down this first domain (e.g., repeatedly multiplying all the distances from the focal point by a given factor, say, $1/2$ or $1/4$). (2) An independent grid can be generated on each domain, assuming that the consistent refinement property is satisfied, i.e., the maximum distance across a grid cell is scaled down with the same rate as the diameter of the contracted domains.

The "scaled-grid" approach (sketch (a) in Figure 2) is especially useful for studying interior discretizations and straight boundaries. It is impractical to implement it for studies near a general (discretely defined) curvilinear boundary because the physical boundary shape should be preserved on each grid in the DS sequence (sketch (c) in Figure 2). In the DS test, the studied FVD scheme is supplemented with a set of boundary conditions at the interface between the interior and the DS domain; overspecification from the known manufactured solution is a possible choice. The freedom to choose the focal point, the shape of domains, and the type of boundary conditions greatly simplifies DS testing. In studying accuracy of discrete boundary conditions, i.e., when the focal point is at the physical boundary, the physical conditions are implemented at the studied

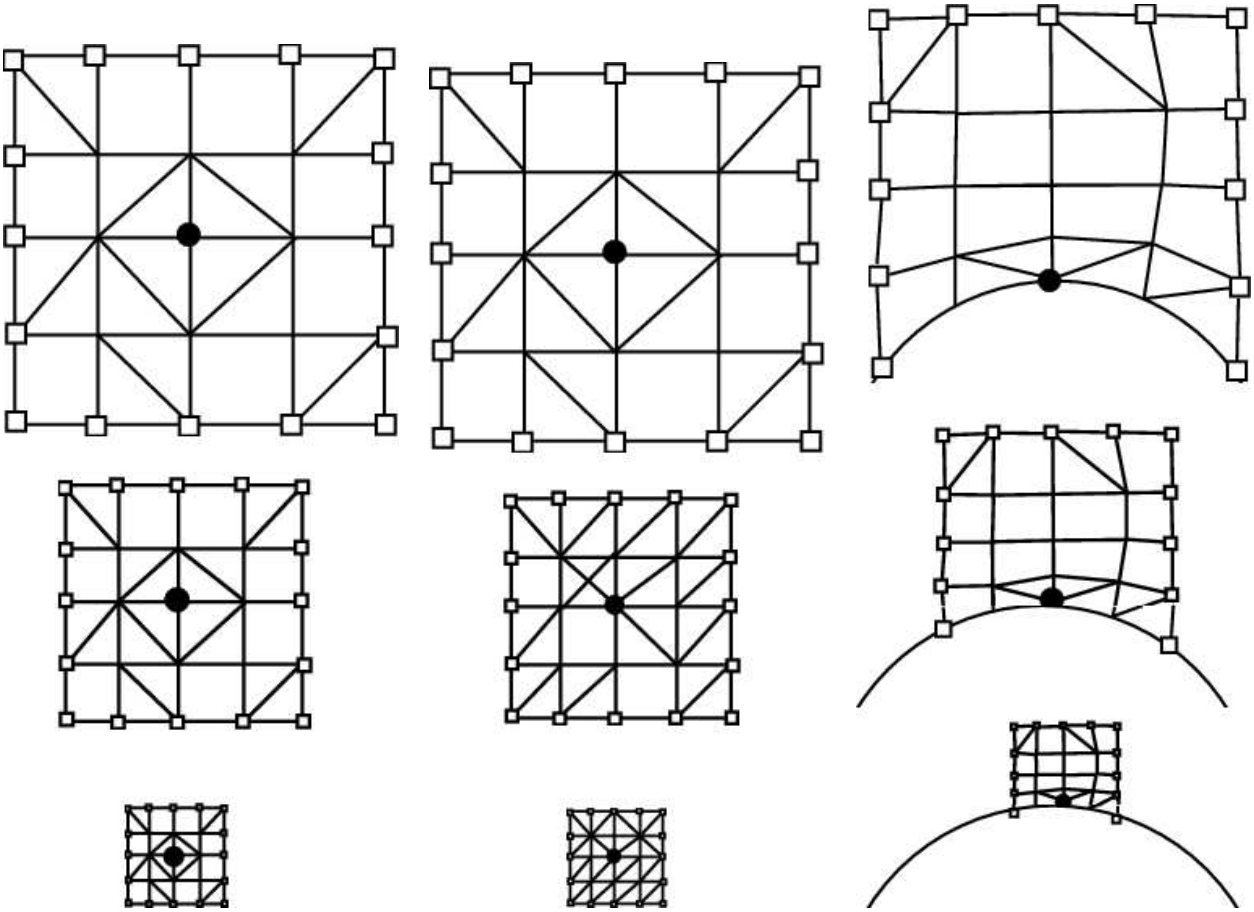

(a) Scaled grid

(b) Independent grid generation

(c) Accounting for curved physical boundary

Figure 2: *DS test: illustration of computational domains for studying the interior and general boundary. Black bullets mark the focal points; white squares mark the interface between the interior and the DS-test domain.*

boundary surface; overspecification can be applied at the interface between the interior and the DS domain (see sketches in Figure 2).

The DS test evaluates local truncation and discretization-error convergence orders by comparing errors obtained in computations on different scales. The DS convergence of truncation errors is a precise indication of the truncation-error convergence (in the L_∞-norm) observed in global grid-refinement computations, as long as the DS test samples all representative regions. Global convergence in integral norms, e.g., L_1-norm, may be higher order because these norms are less sensitive to fluctuations occurring locally.

On grids with an increased regularity, the DS test may overestimate convergence of the discretization errors. Some global error accumulation can occur on such grids; because of its local nature and overspecified interface boundary conditions, the DS test is incapable to account for the global error accumulation. Our experience shows that on truly unstructured multidimensional grids, errors produced locally dominate globally accumulated errors, and the discretization-error

estimates obtained in a DS test become sharp.

3 ANALYSIS OF DS-TEST DISCRETIZATION AND TRUNCATION ERRORS

In this section, we describe an analytical approach to estimating the convergence orders of the discretization and truncation errors observed in DS tests on general unstructured grids. The analysis provides conservative estimates; typically on regular grids, the truncation-error convergence rates are higher because of local error cancellations.

The discrete conservation-law equations are

$$\oint_{\Gamma} \left(\mathbf{F^h}\left(Q^h\right)\cdot\hat{\mathbf{n}}\right)\, d\Gamma = \iint_{\Omega} \left(f^h - S^h\left(Q^h\right)\right)\, d\Omega, \tag{6}$$

where the flux reconstruction $\mathbf{F^h}$ and the source approximation S^h depend on the node-centered discrete solution, Q^h; outward normal $\hat{\mathbf{n}}$, the discrete force function f^h, and all integrals are approximated with certain accuracy by predefined methods. Assuming the discretization error to be small comparing to the exact solution, Q, ($|E_d| << |Q|$), the discretization error can be evaluated as

$$E_d \approx J^{-1}(Q)R(Q), \tag{7}$$

where $R\left(Q\right)$ and $J\left(Q\right)$ are the residual and the Jacobian of the discrete conservation law, respectively;

$$\begin{aligned} R(Q) &= \tfrac{1}{|\Gamma|}\left[-\oint_{\Gamma}\left(\mathbf{F^h}\left(Q\right)\cdot\hat{\mathbf{n}}\right)d\Gamma + \iint_{\Omega}\left(f^h - S^h\left(Q\right)\right)d\Omega\right], \\ J\left(Q\right) &= \tfrac{\partial}{\partial Q}\left(\tfrac{1}{|\Gamma|}\left[\oint_{\Gamma}\left(\mathbf{F^h}\left(Q\right)\cdot\hat{\mathbf{n}}\right)d\Gamma + \iint_{\Omega} S^h\left(Q\right)d\Omega\right]\right), \end{aligned} \tag{8}$$

$|\Gamma| = |\Omega|^{(d-1)/d} = h^{d-1}$ is the measure of the control-volume boundary, where d is the space dimension and h is a characteristic diameter of the control volumes. Note, that in distinction from (4), $R(Q)$ is the residual of an *integral* conservation law and as such is normalized with $|\Gamma|$, not $|\Omega|$. The truncation error relates to $R(Q)$ as

$$E_t = \frac{R(Q)}{h}. \tag{9}$$

For general *systems* of nonlinear equations, the asymptotic order, m_J, of $J^{-1}(Q) = O(h^{m_J})$ can be predicted by analyzing an *equivalent linear operator*, $E(Q)$, that is derived from the $J(Q)$ operator (8) by formally replacing all spatial derivative operators contributing to the Jacobian with $O(1/h^k)$ terms, where k is the differentiation order. With this approach, terms like $\oint_{\Gamma}\left(g(Q)n_x\right)\, d\Gamma$ are replaced with $g(Q)O(h^{d-1})$ and terms like $\iint_{\Omega} g(Q)\, d\Omega$ are replaced with $g(Q)O(h^d)$; here $g(Q)$ is a functional of the (manufactured) solution and/or its derivatives and n_x is the x-directional component of the outward normal $\hat{\mathbf{n}}$. We will refer to these replacements as *equivalent substitutions*. After equivalent substitutions, $E(Q)$ can be inverted to estimate the order of $J^{-1}(Q)$. For basic fluid equations, this analytical evaluation can be performed with relative ease, as shown in subsequent examples. For more complicated equations, the DS test can be expanded to evaluate $J^{-1}(Q)$ numerically.

A scalar (nonlinear) equation is called *non-degenerated* for a given manufactured solution, if the coefficients of the leading terms in the equation linearized around this solution do not all vanish. For FVD schemes discretizing non-degenerated scalar conservation laws with zero source function S, a simple rule for evaluating the asymptotic order of $J^{-1}(Q) = O(h^{m_J})$ is

$$m_J = (\text{order of solution differentiation in } \mathbf{F}). \tag{10}$$

The asymptotic order of the discretization error also depends on the $R(Q)$ approximation order, m_R, $R(Q) = O(h^{m_R})$. There are four main contributors determining the accuracy of $R(Q)$: (1) flux reconstruction, (2) control-volume boundary approximation, (3) flux integration, and (4) source and forcing term integration. Note that the contributors (1)-(3) have also been identified in [14]. A p^{th}-order accuracy for $R(Q)$ ($m_R = p$) can be achieved, if the following four *sufficient accuracy conditions* are satisfied. The conditions are formulated in terms of the maximal degree of a polynomial, for which the considered approximation provides the precise outcome.

1. Flux reconstruction accuracy The flux $\mathbf{F^h}$ should be reconstructed precisely at the control-volume boundaries for an analytical flux F represented by polynomials of the $(p-1)^{th}$ degree.

2. Control-volume boundary accuracy The integral of the outward normal to the boundary should be computed precisely for each boundary segment represented as a $(p-1)^{th}$-order curve, i.e., its (piecewise) parametric formulation with respect to the curve length involves only polynomials of the $(p-1)^{th}$ degree. In many practical cases, the control volumes in the interior have piecewise linear boundaries, so this contributor plays an important role only near the physical boundaries of the computational domain, where the imposed geometry must be approximated.

3. Flux integration accuracy The flux integration method should be exact for fluxes represented as polynomials of the $(p-1)^{th}$ degree. Note that this condition relates to the accuracy of the integration scheme, and assumes no reconstruction errors. In particular, in 1D FVD schemes, this condition is satisfied for all polynomials because each of the two control-volume boundaries collapse to a single point. In multiple dimensions, one should distinguish between the global and local integration accuracies. The *global* p^{th}-order integration accuracy is achieved when the numerical integration of polynomials of $(p-1)^{th}$ degree over the entire closed control-volume boundary is exact, i.e., provides the same result as the analytical integration. To achieve the *local* integration accuracy of p^{th} order, the $(p-1)^{th}$ degree polynomials should be integrated exactly over each segment of the boundary. Local accuracy is more strict and implies global accuracy of the same order or higher; global p^{th}-order flux integration accuracy is sufficient. For many FVD schemes, local and global flux integration accuracies are the same, however, one commonly used FVD scheme discussed in Section 5.2.2 relies on an economic integration strategy that capitalizes on the global integration accuracy order exceeding the order of the local integration accuracy.

4. Source and forcing term integration accuracy The integral over the control volume should be computed precisely for the integrated function represented by a polynomial of the $(p-2)^{th}$ degree.

Each of these sufficient accuracy conditions can be evaluated separately and independently. Note: (1) the flux reconstruction and flux integration conditions recover the steps given in [4] for

linear and quadratic schemes on unstructured meshes; (2) these conditions are conservative (not necessary) because higher-order approximation to $R\,(Q)$ can be achieved due to error cancellation, especially, on regular (structured) grids. For conservation laws, with $J^{-1}(Q) = O(h^{m_J})$ and $R\,(Q) = O(h^{m_R})$, the truncation and discretization errors are evaluated as

$$E_t = O(h^{m_R-1}) \text{ and } E_d = O(h^{m_R+m_J}). \tag{11}$$

The following chart summarizes relations between error convergence orders predicted by analytical estimates (11), observed in DS tests, and observed in global grid-refinement computations. The analytical estimates (11) predict error convergence observed in DS tests; the estimates are conservative because they do not account for possible error cancellation occurring on regular grids. The DS test is designed to predict the convergence orders observed in global computations. The tests provide exact estimates for truncation error convergence, but do not account for possible discretization-error accumulation. On truly unstructured multidimensional grids, both the estimates (11) and the DS-test estimates proved to be sharp.

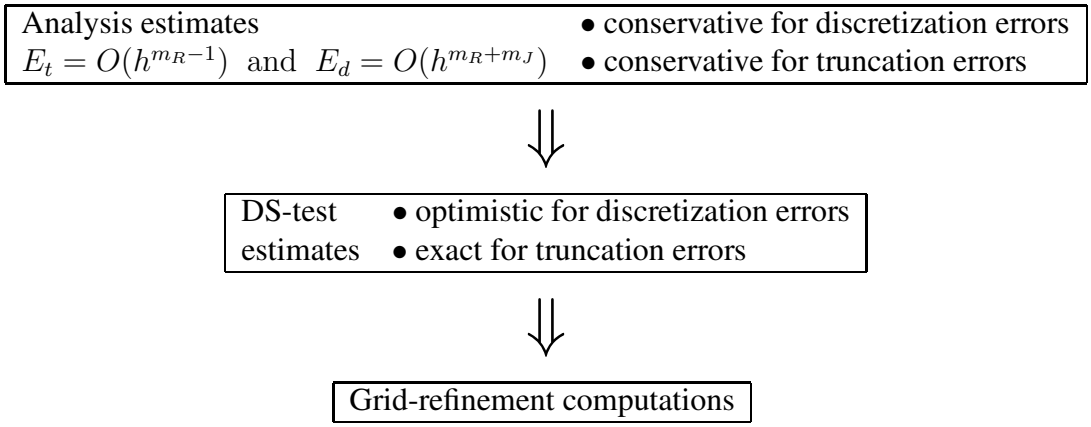

4 ONE-DIMENSIONAL EXAMPLES

For one-dimensional (1D) equations, sufficient conditions for control-volume boundary accuracy and for flux-integration accuracy (conditions 2 and 3 in Section 3) are automatically satisfied. For simplicity, the examples considered in this section do not have source terms and the forcing term is integrated analytically, so m_R is fully determined by the accuracy of the flux reconstruction.

4.1 Discretization grids

A 1D discretization grid is defined as a combination of the primal and dual nodes. The solution values are located at the primal nodes; the fluxes are located at the dual nodes. For node-centered discretizations, a natural strategy is to place the primal mesh first and, then, use this mesh as a reference for placing dual control volumes.

The 1D node-centered discretization grids employed in this section are designed to study effects of grid irregularities and are described as follows. The first and the last of the $N+1$ primal nodes, $x_i, i = 0, 1, \ldots, N$, are always located at the ends of the computational interval; the interior nodes can be distributed either uniformly or randomly. Either distribution retains the nodal ordering and ensures that the maximal distance between the neighboring nodes is $O(1/N)$. Let $s_i, i =$

$0, 1, \ldots, (N+1)$ denote the flux locations. The first and the last fluxes are also located at the ends of the interval; the location of an interior flux, s_i, is always between the primal nodes x_{i-1} and x_i and initially defined as either a biased or an unbiased average; then, the dual node s_i may be randomly perturbed.

(a) Uniform primal mesh; unperturbed unbiased dual mesh

(b) Uniform primal mesh; perturbed unbiased dual mesh

(c) Random primal mesh; unperturbed unbiased dual mesh

Figure 3: *Examples of one-dimensional discretization grids: black bullets denote primal mesh nodes, vertical tic-marks denote dual mesh nodes*

Specifically, on an interval $x \in [a,\, b]$, the primal nodes are distributed according to

$$x_0 = a; \quad x_i = a + (i + r_i)\,\frac{b-a}{N}, \quad i = 1, \ldots, (N-1); \quad x_N = b; \tag{12}$$

where r_i is either zero (uniform primal mesh) or a random number $-0.4 \le r_i \le 0.4$ (random primal mesh). The dual-mesh nodes are computed accordingly as

$$s_0 = a; \quad s_i = x_{i-1} + d_i\,(x_i - x_{i-1})\,, \quad i = 1, \ldots, N; \quad s_{N+1} = b; \tag{13}$$

where $d_i = 0.5$ corresponds to an unbiased unperturbed dual mesh; $d_i = 0.7$ corresponds to a biased unperturbed dual mesh; and $d_i = 0.5 + r_i^s$ or $d_i = 0.7 + r_i^s$ correspond to unbiased and biased perturbed dual meshes, respectively; here r_i^s is a random number $-0.25 \le r_i^s \le 0.25$. Grid examples are shown in Figure 3. Note, that multidimensional median-dual partition can be characterized as a combination of a random primal mesh and an unbiased, perturbed dual mesh.

The global computations in this section refer to tests performed on the interval $x \in [0,\, 1]$ using a sequence of grids with the total number of grid nodes increasing as $N = 2^3,\, 2^4,\, \ldots,\, 2^{14}$. The DS test is performed on a sequence of the intervals $[0.5 - l,\; 0.5 + l]$, where $l \;= 2^{-1},\, 2^{-2},\, \ldots,\, 2^{-10}$ is a scaling factor; the random grids on each scale are generated independently; the number of grid nodes at each scale is fixed, $N = 16$.

4.2 Convection equation

In the first example concerned with a constant-coefficient convection equation, we illustrate applications of the DS test to predict the accuracy of unstructured FVD schemes. The equation

$$\partial_x U = f(x), \quad U(0) \;= U_0 \tag{14}$$

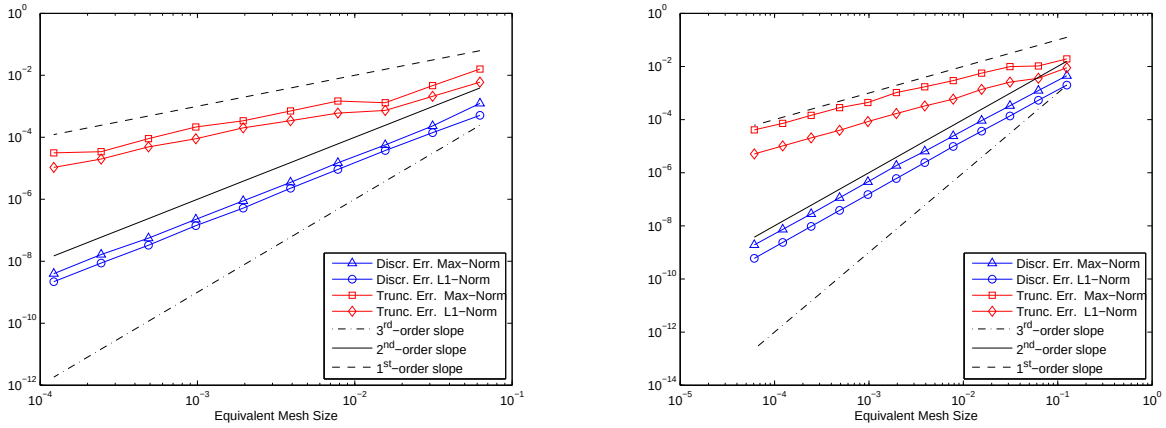

(a) DS test

(b) Grid-refinement computations

Figure 4: *Convergence of discretization and truncation errors for the constant-coefficient convection equation. The tests are performed with random primal meshes and unbiased unperturbed dual meshes.*

is satisfied with the exact solution $U = \sin(x)$, $f = \cos(x)$. This is a constant-coefficient equation and, therefore, non-degenerated. FVD equations are formed as follows

$$F_{s_{i+1}} - F_{s_i} = \sin(s_{i+1}) - \sin(s_i), \qquad i = 0, \ldots, N. \tag{15}$$

The fluxes, F_{s_i}, approximate solution values at the dual nodes, s_i, and are computed by fully-upwind extrapolations from the primal nodes (except for the first interior dual node) as

$$\begin{aligned} F_{s_0} &= U_0, \\ F_{s_1} &= \tfrac{(s_1-x_0)U_1+(x_1-s_1)U_0}{x_1-x_0}, \\ F_{s_i} &= \tfrac{(s_i-x_{i-2})U_{i-1}-(s_i-x_{i-1})U_{i-2}}{x_{i-1}-x_{i-2}}, \quad i = 2, \ldots, N+1 \end{aligned} \tag{16}$$

where U_i is a discrete approximation to $U(x_i)$. These inviscid fluxes do not include solution derivatives and thus, according to (10), $J^{-1}(Q) = O(1)$ in all cases. All fluxes (16) are 2^{nd}-order accurate and, thus, $R(Q) = O(h^2)$. The analysis predicts the discretization error $E_d = O(h^2)$ and the truncation error $E_t = O(h)$.

Figure 4 shows convergence rates obtained in grid-refinement and DS computations on irregular discretization grids involving random primal meshes and unbiased unperturbed dual meshes. The convergence history of the L_∞ and L_1 norms of truncation and discretization errors observed in the global computations confirms the sharp estimates obtained in the DS test. The analysis correctly predicts 2^{nd}-order convergence of discretization errors and 1^{st}-order convergence of truncation errors.

Table 1 summarizes discretization and truncation error convergence rates observed in computations with 1D node-centered FVD schemes. Although not shown, similar convergence rates are observed for cell-centered FVD schemes. The results reveal two important trends valid for general non-degenerated inviscid equations: (1) grid irregularity strongly affects the truncation-error

Table 1: *Convergence of discretization and truncation errors of node-centered FVD schemes for the constant-coefficient convection equation.*

Primal Mesh	Dual Mesh	DS test		Grid-refinement computations	
		Discr. Error	Trunc. Error	Discr. Error	Trunc. Error
Uniform	Unbiased, Unperturbed	$O(h^2)$	$O(h^2)$	$O(h^2)$	$O(h^2)$
Uniform	Biased, Unperturbed	$O(h^2)$	$O(h^2)$	$O(h^2)$	$O(h^2)$
Uniform	Unbiased Perturbed	$O(h^2)$	$O(h)$	$O(h^2)$	$O(h)$
Uniform	Biased Perturbed	$O(h^2)$	$O(h)$	$O(h^2)$	$O(h)$
Random	Unbiased, Unperturbed	$O(h^2)$	$O(h)$	$O(h^2)$	$O(h)$
Random	Biased, Unperturbed	$O(h^2)$	$O(h)$	$O(h^2)$	$O(h)$
Random	Unbiased, Perturbed	$O(h^2)$	$O(h)$	$O(h^2)$	$O(h)$
Random	Biased, Perturbed	$O(h^2)$	$O(h)$	$O(h^2)$	$O(h)$

convergence, but has no effect on convergence of the discretization errors; (2) bias does not affect convergence rates. The analysis estimates are sharp for discretization errors on all grids and for truncation errors on all "randomized" grids. The convergence of truncation errors on uniform unperturbed grids is 2^{nd} order because of error cancellations occurring on these regular grids. The DS-test convergence rates are precise indicators of the rates observed in global computations.

4.3 Diffusion equation

The second set of one-dimensional tests illustrates the application of the DS analysis methodology to the diffusion equation or, more generally, to any FVD scheme, in which fluxes include solution derivatives. The non-degenerated constant-coefficient diffusion equation

$$\partial_{xx}U = f(x), \quad U(0) = \bar{U}_0, \quad U(1) = \bar{U}_1, \tag{17}$$

is defined on the interval $x \in [0,\ 1]$, with the exact solution $U = \sin(x)$, $f = -\sin(x)$. FVD equations are formed as

$$F_{s_{i+1}} - F_{s_i} = \cos(s_{i+1}) - \cos(s_i), \quad i = 1, \ldots, N; \quad U_0 = \bar{U}_0; \quad U_N = \bar{U}_1. \tag{18}$$

Fluxes approximating the solution derivative are defined as

$$F_{s_i} = \frac{U_i - U_{i-1}}{x_i - x_{i-1}}, \quad i = 1, \ldots, N, \tag{19}$$

where U_i is a discrete approximation to $U(x_i)$. Dirichlet boundary conditions are enforced. According to (10), $J^{-1}(Q) = O(h)$.

Table 2: *Convergence of discretization and truncation errors of node-centered FVD schemes for the diffusion equation.*

Primal Mesh	Dual Mesh	DS test		Grid-refinement computations	
		Discr. Error	Trunc. Error	Discr. Error	Trunc. Error
Uniform	Unbiased, Unperturbed	$O(h^4)$	$O(h^2)$	$O(h^2)$	$O(h^2)$
Uniform	Biased, Unperturbed	$O(h^3)$	$O(h)$	$O(h)$	$O(h)$
Uniform	Unbiased, Perturbed	$O(h^2)$	$O(1)$	$O(h^2)$	$O(1)$
Uniform	Biased, Perturbed	$O(h^2)$	$O(1)$	$O(h)$	$O(1)$
Random	Unbiased, Unperturbed	$O(h^3)$	$O(h)$	$O(h^2)$	$O(h)$
Random	Biased, Unperturbed	$O(h^2)$	$O(1)$	$O(h)$	$O(1)$
Random	Unbiased, Perturbed	$O(h^2)$	$O(1)$	$O(h^2)$	$O(1)$
Random	Biased, Perturbed	$O(h^2)$	$O(1)$	$O(h)$	$O(1)$

The placement of dual nodes (flux locations) significantly affects the error convergence. For unbiased, unperturbed dual meshes, the fluxes are approximated with the 2^{nd}-order accuracy, thus, providing $R(Q) = O(h^2)$. For such FVD schemes, the analysis predicts the discretization error $E_d = O(h^3)$ and the truncation error $E_t = O(h)$. For either perturbed or biased dual meshes, $R(Q)$ is approximated with the 1^{st}-order accuracy, and the corresponding estimates are $E_d = O(h^2)$ and $E_t = O(1)$.

Table 2 summarizes the discretization and truncation error convergence rates observed for 1D node-centered FVD schemes. The two main observations about grid-refined convergence rates of discretization errors are (1) local "random" grid irregularities do not affect the discretization-error convergence and (2) grid bias leads to one-order convergence deterioration.

The analytical estimates for the DS-test convergence rates are sharp for all grid types except uniform-primal/unperturbed-dual type; the convergence rates on these grids are faster because of local error cancellation. The DS tests accurately predict convergence orders of grid-refinement truncation errors. The discretization-error convergence order is predicted well for the unbiased perturbed dual meshes, but overestimated in other cases. The reason for this overestimation is the error accumulation occurring in grid-refinement computations for all dual meshes except the unbiased perturbed type. Note that the latter type is representative of multidimensional median-dual partitions. Based on experience to date, in multidimensional computations on general unstructured grids, the estimates obtained in DS tests are sharp as shown in following sections.

5 TWO-DIMENSIONAL COMPUTATIONS

5.1 Poisson equation

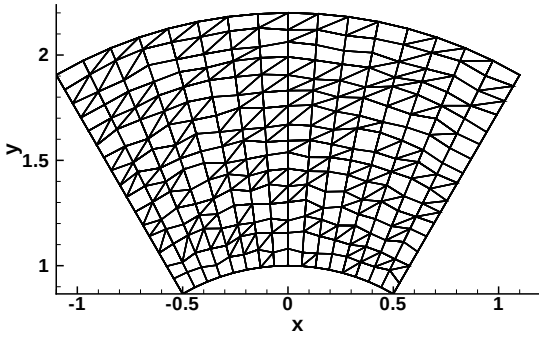

Figure 5: *A typical mixed-element unstructured grid generated with random splitting and random perturbation of the underlying quadrilateral grid.*

As a two-dimensional scalar example, we solve the Poisson equation,

$$\Delta U = f, \tag{20}$$

with Dirichlet boundary conditions, on a series of primal mixed-element grids composed of triangles and quadrangles. Each grid is formed from an underlying structured quadrilateral grid (Figure 5). In terms of a polar, (r, θ), coordinate system, the grid extent is defined as $\theta \in [\pi/6, \pi/3]$ in the circumferential direction and $r \in [1, 2.2]$ in the radial direction. The decision to split (or not to split) each structured quadrangle into triangles is determined randomly; approximately half of the quadrilaterals are split. In addition, the interior grid points are perturbed from their original position by random shifts in the range $[-\sqrt{2}/6, \sqrt{2}/6]$ of the local mesh size in the radial direction.

The exact solution and forcing term are taken as $U = [(\sin(\pi x))^2 + (\sin(\pi y))^2]/2$, $f = -2\pi^2[1 - (\cos(\pi x))^2 - (\cos(\pi y))^2]$. In the FVD scheme, the solution is represented as a piecewise polynomial function, with polynomials defined at the primal cells; the conservation law

$$\oint_{\Gamma} \nabla \mathbf{U} \cdot \hat{\mathbf{n}} \, d\Gamma = \iint_{\Omega} f \, d\Omega \tag{21}$$

is enforced on node-centered control volumes constructed by the median-dual partition.

With reference to Figure 6, the integral flux through the dual faces adjacent to the edge $[P_0, P_4]$ is computed as

$$\int_{ABC} \nabla \mathbf{U} \cdot \hat{\mathbf{n}} \, d\Gamma = \nabla \mathbf{U}^R \cdot \mathbf{n_R} + \nabla \mathbf{U}^L \cdot \mathbf{n_L}, \tag{22}$$

where $\mathbf{n_R}$ and $\mathbf{n_L}$ are directed areas of the corresponding dual faces. The gradient is reconstructed separately at each dual face as follows.

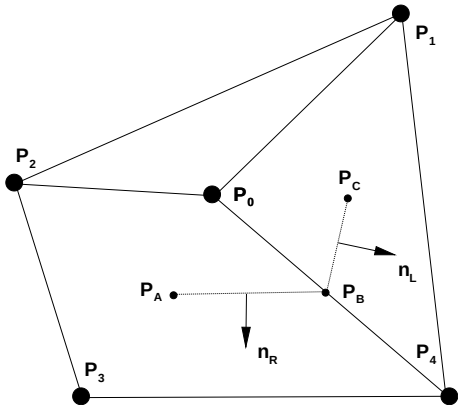

Figure 6: *Illustration of gradient reconstruction for viscous terms on mixed grids with median-dual partition.*

For the triangular element contribution, the gradient is determined from a Green-Gauss evaluation at the primal-grid element,

$$\nabla \mathbf{U}^L = \overline{\overline{\nabla \mathbf{U}}}_{014}. \tag{23}$$

The gradient overbar denotes a gradient evaluated by the Green-Gauss formula on the primal cell identified by the point subscripts. With fully-triangular elements, the formulation is equivalent to a Galerkin finite element scheme with a linear basis function [2, 3]. For the quadrilateral element contribution, the gradient is evaluated as

$$\nabla \mathbf{U}^R = \overline{\overline{\nabla \mathbf{U}}}_{0234} + \left[\frac{U_4 - U_0}{|\mathbf{r}_4 - \mathbf{r}_0|} - \overline{\overline{\nabla \mathbf{U}}}_{0234} \cdot \mathbf{e}_{04} \right] \mathbf{e}_{04}, \tag{24}$$

where $\mathbf{r}_i$ is the coordinate vector of node P_i and

$$\mathbf{e}_{04} = \frac{\mathbf{r}_4 - \mathbf{r}_0}{|\mathbf{r}_4 - \mathbf{r}_0|} \tag{25}$$

is the unit vector aligned with the edge $[P_0, P_4]$. Note that for grids with dual faces perpendicular to the edges, the edge-gradient is the only contributor. This approach to the gradient reconstruction is used to decrease the scheme susceptibility to odd-even decoupling [7, 8]. In all cases, the linear solution reconstruction leads to the 1^{st}-order flux (gradient) reconstruction accuracy.

The asymptotic order of $J^{-1}(Q)$, computed according to (10), is $m_J = 1$. The volume integral of the forcing term in (21) is evaluated as the value at the node multiplied by the dual volume. Overall, $R(Q) = O(h)$. The analysis predicts the discretization error $E_d = O(h^2)$ and the truncation error $E_t = O(1)$.

The sequences of globally refined grids are generated with $2^{n+3} + 1$ points in both the radial and circumferential directions, where $n = 0,\ 1,\ 2,\ 3,\ 4$. The sequences of DS grids are generated from a grid with 17 points in both the nominal radial and circumferential directions and downscaled about the center of the domain by a factor 2^{-s}, where $s = 0,\ 2,\ 4,\ 6,\ 8$. The grid topology remains unchanged.

The L_1 norms of truncation and discretization errors are shown in Figure 7 versus an equivalent mesh size parameter, taken as the L_1 norm of the square root of the dual volume. Although not

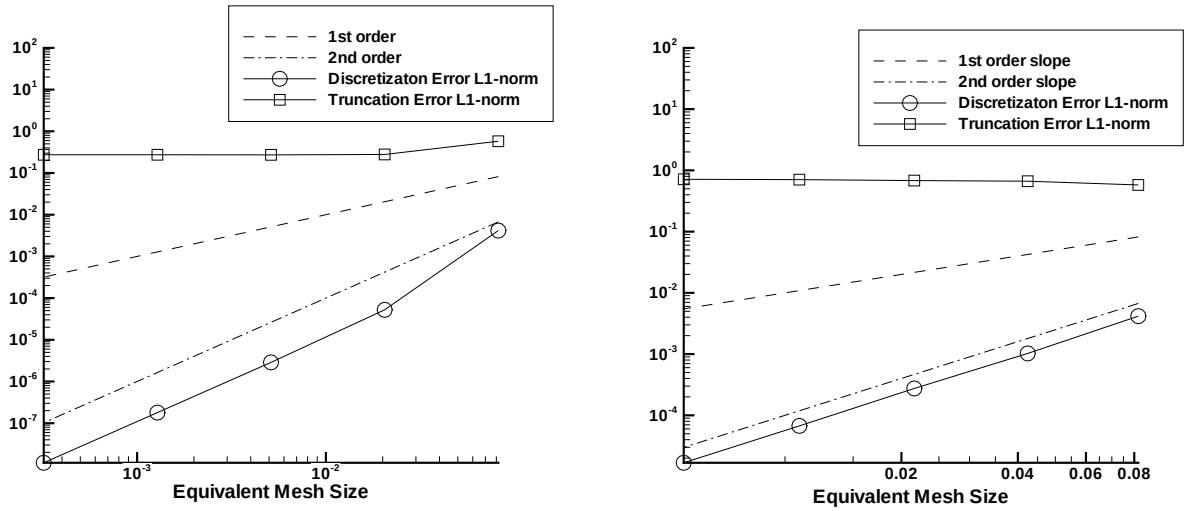

(a) DS test

(b) Grid refinement computations

Figure 7: *Convergence of the discretization and truncation errors for the Poisson equation solved on irregular mixed-element unstructured grids.*

shown, error convergence rates in the L_∞ norm are the same as the L_1-norm rates. The analysis predicts the DS-test error convergence rate precisely. In grid-refinement computations, the truncation errors remain $O(1)$ and the discretization errors converge with 2^{nd}-order, precisely predicted by the DS test. The reason for the $O(1)$ convergence of truncation errors is grid irregularity stemming from the perturbation to the grid points and the usage of mixed grids. Both references [11] and [17] interpret $O(1)$ convergence of truncation errors on irregular grids as indication that the corresponding discrete solutions do not approximate the continuous ones; this example clearly shows that this is not the case.

Although not shown, with no perturbations and with meshes composed of either regular triangles alone or regular quadrangles alone, both the truncation errors and the discretization errors converge with 2^{nd} order in grid-refinement and DS-test computations.

5.2 Incompressible Euler equations

In this section we consider incompressible inviscid equations. The source function S is assumed to be zero. Inviscid fluxes for conservation of mass and momentum are defined as

$$\mathbf{F} = \mathbf{f}\bar{\mathbf{i}} + \mathbf{g}\bar{\mathbf{j}} = \begin{bmatrix} \beta u \\ u^2 + p \\ uv \end{bmatrix} \bar{\mathbf{i}} + \begin{bmatrix} \beta v \\ uv \\ v^2 + p \end{bmatrix} \bar{\mathbf{j}}, \tag{26}$$

where the vector of unknowns, $Q = [u, v, p]$, includes the Cartesian velocities and the pressure; β is an artificial compressibility parameter introduced as in [2] and taken as $\beta = 1$ here.

The median-dual partition is applied. At each dual control volume, a polynomial solution approximation is constructed. The approximation is required to coincide with the discrete solution value at the central node P_0; the polynomial coefficients are determined through a least-square pro-

cedure involving neighboring nodes, i.e., nodes linked by an edge to the central node P_0. If the set of neighboring nodes is insufficient to determine, uniquely and stably, the polynomial coefficients, the set may be expanded to involve neighbors of neighbors. Three node-centered FVD schemes are considered: an edge-reconstruction scheme and two face-reconstruction schemes.

5.2.1 Equivalent linear operator

The Jacobian of $\oint_\Gamma (\mathbf{F}\cdot\hat{\mathbf{n}})\, d\Gamma$ is a 3×3 matrix

$$\oint_\Gamma \begin{pmatrix} n_x & n_y & 0 \\ 2un_x + vn_y & un_y & n_x \\ vn_x & un_x + 2vn_y & n_y \end{pmatrix} d\Gamma \tag{27}$$

operating on the vector $\delta Q = [\delta u, \delta v, \delta p]^T$. After equivalent substitutions, the equivalent linear operator, $E(Q)$, becomes

$$E(Q) = \begin{pmatrix} O(1) & O(1) & 0 \\ uO(1) + vO(1) & uO(1) & O(1) \\ vO(1) & uO(1) + vO(1) & O(1) \end{pmatrix}. \tag{28}$$

If $u^2+v^2 > \varepsilon > 0$ everywhere in the computational domain, i.e., the equations are non-degenerated, the inverse of $E(Q)$ is a full matrix

$$J^{-1}(Q) \sim E^{-1}(Q) = \begin{pmatrix} O(1) & O(1) & O(1) \\ O(1) & O(1) & O(1) \\ O(1) & O(1) & O(1) \end{pmatrix}. \tag{29}$$

In a general situation, the asymptotic order of $J^{-1}(Q)$ can be different for different equations, but for non-degenerated inviscid equations, the asymptotic order is $m_J = 0$ for all three equations. The effect of degeneration on convergence of the discretization errors is considered subsequently in Section 5.3. In the course of Section 5.2, we assume non-degenerated equations implying non-vanishing velocity components of the (manufactured) solution.

5.2.2 Edge-reconstruction scheme

This FVD scheme is commonly used in unstructured computations [2, 3, 7, 8, 11]. By construction, the dual boundaries are piecewise linear and, therefore, in the interior and next to straight boundaries, the outward normal $\hat{\mathbf{n}}$ approximation contributes no error to $R(Q)$. The numerical upwind flux at the edge midpoint is approximated according to the Roe scheme [2, 16],

$$\left(\mathbf{F^h}\cdot\hat{\mathbf{n}}\right) = \frac{1}{2}\left[(\mathbf{F_0}\cdot\hat{\mathbf{n}}) + (\mathbf{F_1}\cdot\hat{\mathbf{n}})\right] - \frac{1}{2}\left|\mathbf{A}(\bar{\mathbf{Q}})\right|(\mathbf{Q_1} - \mathbf{Q_0}), \tag{30}$$

where, $\mathbf{Q_0}$ and $\mathbf{Q_1}$ are the "left" and "right" solution reconstructions at the edge midpoint derived from the linear approximations at the control volumes centered at P_0 and P_1, respectively (see Figure 8); $\mathbf{F_0}$ and $\mathbf{F_1}$ are the corresponding "left" and "right" numerical fluxes; $\hat{\mathbf{n}}$ is the unit vector aligned with the combined-directed-area vector $\mathbf{n} = \mathbf{n_L} + \mathbf{n_R}$, where $\mathbf{n_L}$ and $\mathbf{n_R}$ are outward

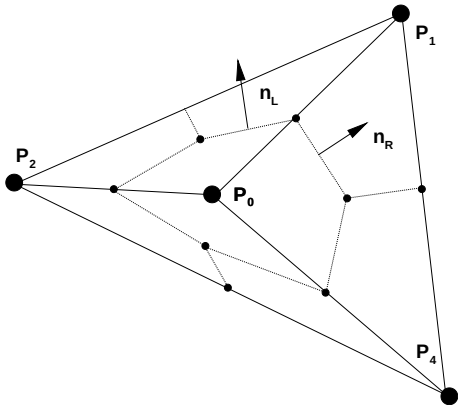

Figure 8: *Illustration for edge-reconstruction flux integration scheme in the interior.*

normal (directed-area) vectors of the left and right segments, respectively, with their amplitudes equal to the corresponding segment lengths; $\left|\mathbf{A}(\bar{\mathbf{Q}})\right|$ is the Roe's approximate Riemann solver matrix computed for $\bar{\mathbf{Q}} = \frac{1}{2}(\mathbf{Q_1} + \mathbf{Q_0})$. With a linear solution approximation at each control volume, this is a 2^{nd}-order accurate flux reconstruction.

The flux integration over the two segments of the control-volume boundary linked at the edge midpoint is approximated by multiplying $\mathbf{F^h}$ computed at the edge midpoint with the amplitude of the combined-directed-area vector, $|\mathbf{n}|$. According to the definition introduced in the sufficient flux-integration accuracy condition (condition 3 in Section 3), this computationally efficient integration scheme provides 1^{st}-order local integration accuracy. On general triangular grids, the global integration accuracy has been shown to be 2^{nd} order [2, 3, 4], providing the exact integration for the conservation laws with linear fluxes. The edge-reconstruction scheme exhibits similar (1^{st}-order local and 2^{nd}-order global) flux integration accuracy on rectangular grids. On general (irregular) quadrilateral and mixed-element grids, the global flux integration accuracy deteriorates to 1^{st} order. Examples confirming the integration accuracy deterioration on grids composed of quadrilateral and triangular elements are shown in Appendix B

The forcing term integration over the control volume is approximated as the node value multiplied by the volume $|\Omega|$. This approximation is precise for the integral of a constant (zeroth-order polynomial) forcing term. The overall approximation accuracy for $R(Q)$ is $R(Q) = O(h^2)$ on triangular grids and $R(Q) = O(h)$ on general quadrilateral and mixed-element grids, leading to estimates of $E_d = O(h^2)$ and $E_t = O(h)$ for triangular grids and $E_d = O(h)$ and $E_t = O(1)$ for general grids.

For the edge-reconstruction discretization, the boundary is approximated as a piecewise straight line connecting the grid nodes located at the physical boundary. The control volume around a boundary node, P_0, (see Figure 9) is closed with the boundary segments $[P_B, P_0]$ and $[P_0, P_C]$. The straight-line approximation $[P_0, P_2]$ provides a 2^{nd}-order accuracy to the curved boundary segments connecting nodes P_0 and P_2. However, the approximation $[P_0, P_B]$ provides only a 1^{st}-order accuracy for the $\widehat{P_0, P_F}$ part of the curved boundary segment. The flux reconstruction and integration over the segments $[P_A, P_E]$ and $[P_E, P_D]$ are the same as for the interior edges. The integral fluxes through segments $[P_A, P_B]$ and $[P_D, P_C]$ are approximated by the numerical fluxes (30) evaluated at points P_B and P_C using the directed areas $\mathbf{n}_1$ and $\mathbf{n}_4$, respectively. The linear solution approximation at control volumes ensures 2^{nd}-order flux reconstruction accuracy.

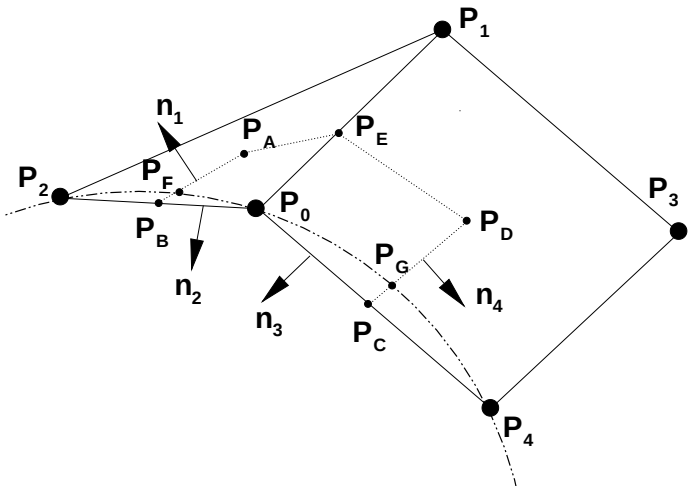

Figure 9: *Illustration for edge-reconstruction flux integration scheme near the boundary.*

Boundary conditions are enforced weakly through the boundary fluxes. The inflow boundary conditions are implemented by evaluating velocity contributions to the boundary flux from prescribed conditions; the outflow boundary conditions are implemented analogously by evaluating pressure boundary-flux contributions from prescribed conditions.

The integral flux through the boundary segment $[P_B, P_0]$ located within a triangular cell is computed as $\left(\mathbf{F^h}_{[P_B,P_0]} \cdot \mathbf{n}_2\right)$, where $\mathbf{n}_2$ is the directed area of $[P_B, P_0]$, and $\mathbf{F^h}_{[P_B,P_0]}$ is evaluated at $\bar{P} = 5/6P_0 + 1/6P_2$. The solution components prescribed in the boundary conditions, e.g., zero normal velocity components at tangency, both velocities at inflow, or the pressure at outflow, are specified at $\bar{P}$ from the known exact solution; other components are interpolated to $\bar{P}$ from the endpoints of the segment $[P_2, P_0]$. The integral flux through the boundary segment $[P_C, P_0]$ located within a quadrilateral cell is computed similarly, $\left(\mathbf{F^h}_{[P_C,P_0]} \cdot \mathbf{n}_3\right)$, but $\mathbf{F^h}_{[P_C,P_0]}$ is evaluated at the node P_0. The integration scheme provides 1^{st}-order local accuracy for integrated fluxes through $[P_B, P_0]$ and $[P_0, P_C]$. On general triangular grids, the interpolation coefficients $5/6$ and $1/6$ lead to cancellation of 1^{st}-order errors, providing zero residuals for conservation laws with linear fluxes and, thus, supporting the global 2^{nd}-order flux integration accuracy [3]. The integration procedure described for boundary segments within a quadrilateral cell leads to the 2^{nd}-order global flux integration accuracy on rectangular cells. The accuracy deteriorates to 1^{st} order for irregular quadrilateral cells and for nodes at the interfaces separating general triangular and quadrilateral cells. The overall approximation accuracy for $R(Q)$ computed at the boundary is consistent with the accuracy of the interior FVD scheme, 2^{nd} order for triangular and rectangular grids and 1^{st} order for general irregular grids.

Reliance on error cancellation in providing design-order discretization accuracy may lead to some counterintuitive phenomena. In particular, improving the accuracy of boundary conditions in a way that is not compatible with the flux computations through interior segments can upset the error cancellation balance and, in fact, worsen approximation accuracy of $R(Q)$, at least, locally. In some cases, this local imbalance is compensated by contributions from other boundary segments. The imbalance is especially prominent at the corners where the boundary segments represent different types (e.g., tangency and inflow) of boundaries.

At the tangency boundary, the mass fluxes and velocity contributions to the momentum fluxes are explicitly set to zero. For control volumes at general curved tangency boundaries, the tangency condition is enforced over the straight segments, rather than over the physical curved boundary. The error introduced by this approach can be considered as a flux reconstruction error introduced by enforcing zero velocity over non-tangency boundary segments. As estimated analytically and confirmed numerically in Section 5.2.4, the error is $O(h)$ for each segment of the tangency boundary. Reference [10] investigates an alternative approach, in which other types of boundary conditions are enforced over the straight boundary segments approximating a curved tangency boundary.

5.2.3 Face-reconstruction schemes

In this section, we describe two face-reconstruction FVD schemes that employ the median-dual partition and provide 2^{nd} and 3^{rd} order accuracies on general mixed grids. Similar to the edge-reconstruction scheme, the linear and quadratic polynomials are defined at dual control volumes and coincide with the solutions at the grid nodes. The polynomial coefficients are defined in a least-square procedure involving solutions at the neighboring nodes. In the interior, piecewise straight dual boundaries imply a precise representation for $\hat{\mathbf{n}}$. The schemes described are quite similar to the scheme described by Delanaye and Liu [6] for cell-centered discretizations. As noted therein and shown in Appendix A, the operation counts significantly favor the cell-centered approach for flux integration in three dimensions.

The distinguishing feature of these face-reconstruction schemes is the flux integration procedures ensuring the designed *local* integration accuracy. Extension of 2^{nd}-order accuracy to mixed grids can be achieved with linear polynomials, a modified straight-segment tangency boundary approximation (see Figure 11 and discussion in Section 5.2.4), and a flux integration scheme providing local 2^{nd}-order accuracy. Accuracy of 3^{rd} order requires quadratic polynomials for flux reconstruction, quadratic fit to the curved tangency boundary, an integration scheme with local 3^{rd}-order accuracy, and a 2^{nd}-order accurate scheme for integrating source and force terms.

In the implemented 2D version, a polynomial flux is defined at each segment of the dual control-volume boundary and used in (30). The "left" and "right" solutions, $\mathbf{Q_0}$ and $\mathbf{Q_1}$, are represented by the basic polynomials defined at the adjacent control volumes; numerical fluxes, $\mathbf{F_0}$ and $\mathbf{F_1}$, are analytically computed as products of the corresponding basic polynomials. The dissipation matrix, $\left|\mathbf{A}(\bar{\mathbf{Q}})\right|$, is computed for $\bar{\mathbf{Q}}$, defined as the average of $\mathbf{Q_0}$ and $\mathbf{Q_1}$ evaluated at the segment midpoint. The polynomial flux at this segment is defined according to (30), where all terms, beside $\left|\mathbf{A}(\bar{\mathbf{Q}})\right|$, are polynomials. The scheme with linear polynomials provides 2^{nd}-order accurate flux reconstruction; fluxes reconstructed with quadratic polynomials are 3^{rd}-order accurate.

The inner product of the polynomial flux vector and the outward unit normal vector is integrated over the segment with a numerical Gauss-Legendre quadrature formula employing 1 point for the linear face-reconstruction scheme, and 2 points for the quadratic face-reconstruction scheme. As a convenient debugging tool, one can add one Gaussian point to have total of 2 and 3 points, respectively, per integration segment. With these improved accuracy integrations, the FVD method should provide zero residuals for linear and quadratic manufactured solutions.

The forcing term integration method for the linear face-reconstruction scheme is the same as for the edge-reconstruction scheme, providing sufficient accuracy for 2^{nd}-order approximation of $R(Q)$. For quadratic face-reconstruction scheme, a linear (or piecewise linear) approximation to the forcing term is constructed and integrated at each control volume providing a 3^{rd}-order accurate

approximation to $\frac{1}{|\Gamma|}\iint\limits_{\Omega} f\, d\Omega$. The overall approximation accuracy for $R(Q)$ is 2^{nd} order for the linear polynomials and the 3^{rd} order for quadratic polynomials and does not deteriorate for general unstructured grids. The predictions for the error convergence rates are $E_d = O(h^2)$, $E_t = O(h)$ for the linear polynomials and $E_d = O(h^3)$, $E_t = O(h^2)$ for the quadratic polynomials.

The boundary conditions for the face-reconstruction discretizations are enforced weakly, through boundary fluxes. At inflow and outflow, the computational domain is bounded by a piecewise straight boundary; the solution components are either specified from the exact solution (the velocity is specified at inflow and the pressure is specified at outflow) or represented by the polynomial approximation defined at the adjacent control volume. At tangency, the 2^{nd}-order accuracy can still be achieved with enforcing tangency over piecewise linear segments. (See discussion in Section 5.2.4.) For the 3^{rd}-order accuracy, the physical boundary should be approximated quadratically. In a general case, where the analytical shape of the boundary is unknown, the boundary should be represented as a piecewise polynomial curve providing the required accuracy for the boundary shape.

5.2.4 Numerical tests for non-degenerated flows

Numerical tests presented in this section are performed for 2D inviscid incompressible flows around a cylinder of unit radius centered in the origin. The flow is described by the conservative equations (1) with zero source and forcing terms and fluxes defined in (26). The analytical solution for this problem is known

$$\begin{array}{l} U = U_\infty + \frac{2\sin^2\theta - 1}{r^2} + \partial_y \psi, \\ V = V_\infty + 2\frac{\sin\theta\cos\theta}{r^2} - \partial_x \psi, \\ P = P_\infty - \frac{U^2+V^2}{2}, \end{array} \tag{31}$$

where (r, θ) are the polar coordinates $r^2 = x^2 + y^2,\ \tan\theta = y/x$, and $\psi = -C\ln(r)$ is the stream function with C being a constant characterizing the flow circulation. In the course of this section, the free stream at the infinity is characterized by $U_\infty = 1$, $V_\infty = 0$, $P_\infty = 1.5$, and the zero circulation ($C = 0$) is assumed.

Interior inflow/outflow domains The first set of tests is performed on a computational domain shifted away from the surface of the cylinder: $1.5 \le r \le 4$, $2\pi/3 \le \theta \le 4\pi/3$. Seven formulations are studied: the edge-reconstruction FVD scheme on randomly-split triangular, randomly-perturbed quadrilateral, and random mixed-element grids; and face-reconstruction FVD schemes on randomly-perturbed quadrilateral and random mixed-element grids. Examples of unstructured grids derived from an underlying structured grid are shown in Figure 10. For triangular and mixed-element grids, randomization is introduced through random splitting (or not splitting) of structured quadrilateral cells. Each cell has equal probabilities to introduce either of the two diagonal choices or, for mixed-element grids, no diagonals. For randomly-perturbed quadrilateral grids, structured interior nodes are perturbed from their original position by random shifts in the range $[-\sqrt{2}/6,\ \sqrt{2}/6]$ of the local mesh size in both the radial and circumferential directions.

For each formulation, grid refinement and DS tests are performed. In grid refinements, the underlined structured grid is refined by doubling the number of intervals in the radial and angular directions. In the DS test, the coarsest 9×9 grid is scaled down around the point $r = 2.75,\ \theta = \pi$

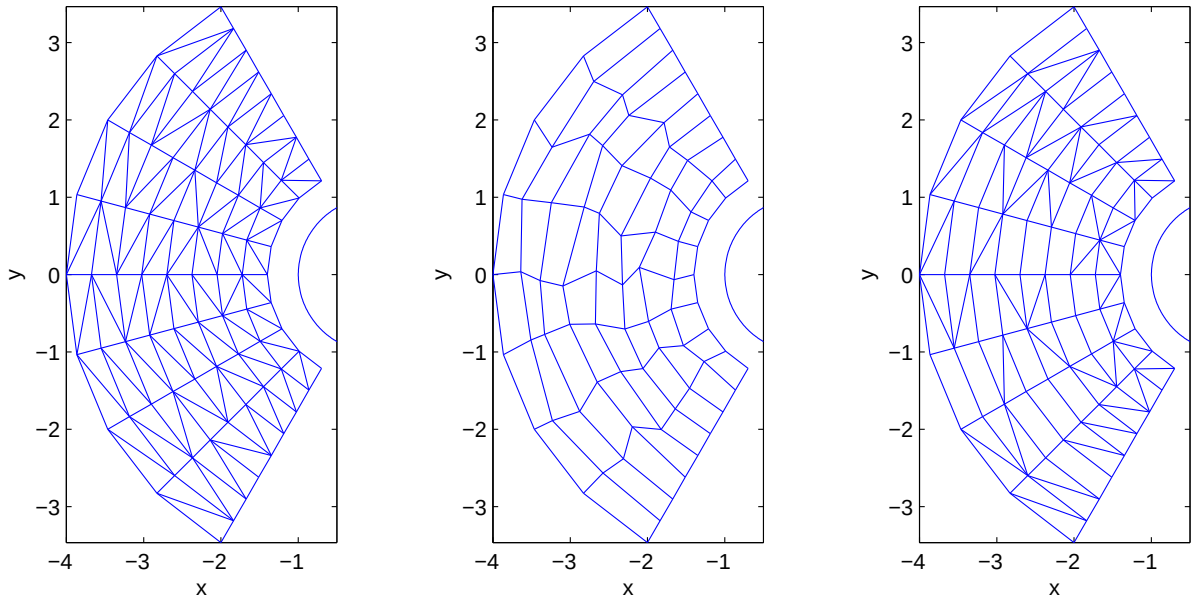

(a) Randomly-split triangular grid

(b) Randomly-perturbed quadrilateral grid

(c) Random mixed-element grid

Figure 10: *Typical triangular and mixed-element unstructured grids defined on a computational domain shifted away from the surface of the cylinder.*

by multiplying all angular and radial deviations from this point by a factor of 0.5. Randomization is introduced independently on each scale. The inflow boundary conditions are enforced at the boundary corresponding to the external radius; outflow conditions are enforced at all other boundaries. Table 3 summarizes the convergence of discretization and truncation errors observed in these tests. Note that the convergence orders are the same in all norms and for all variables and equations. The results confirm analysis predictions and capabilities of the DS test to provide sharp estimates for error convergence in grid refinement computations. The convergence rates observed for the edge-reconstruction scheme on random triangular and random quadrilateral grids are consistent with the results reported in [1]. Although not shown, we have implemented a central version of the edge-reconstruction scheme, where fluxes at the edge midpoints are defined as averages of the solutions in the neighboring nodes. The observed convergence rates were identical with the rates shown in Table 3. The results contradict to [11], where zeroth-order convergence of discretization errors on random quadrilateral grids was reported for a central scheme for a constant-coefficient convection equation. Appendix D provides an in-depth investigation of this discrepancy.

Tangency boundary For the edge-reconstruction FVD scheme on triangular grids, local accuracy deterioration occurs if a curved tangency boundary is approximated by straight segments linking primal-mesh nodes located at the physical boundary. Sketch (a) of Figure 11 illustrates this approximation: the straight segments $[P_2, P_0]$ and $[P_0, P_4]$ approximate a curved boundary, the points P_B and P_C are the segments' midpoints, and the arrow indicates the local flow velocity. For

Table 3: *Convergence of discretization and truncation errors for various unstructured grid formulation of the 2D inviscid incompressible equations on an inflow/outflow computational domain.*

Formulation	DS test		Grid-refinement computations	
	Discr. Err.	Trunc. Err.	Discr. Err.	Trunc. Err.
Edge-reconstruction, randomly-split triangular grid	$O(h^2)$	$O(h)$	$O(h^2)$	$O(h)$
Edge-reconstruction, randomly-perturbed quadrilateral grid	$O(h)$	$O(1)$	$O(h)$	$O(1)$
Edge-reconstruction, random mixed-element grid	$O(h)$	$O(1)$	$O(h)$	$O(1)$
Linear face-reconstruction, randomly-perturbed quadrilateral grid	$O(h^2)$	$O(h)$	$O(h^2)$	$O(h)$
Linear face-reconstruction, random mixed-element grid	$O(h^2)$	$O(h)$	$O(h^2)$	$O(h)$
Quadratic face-reconstruction, randomly-perturbed quadrilateral grid	$O(h^3)$	$O(h^2)$	$O(h^3)$	$O(h^2)$
Quadratic face-reconstruction, random mixed-element grid	$O(h^3)$	$O(h^2)$	$O(h^3)$	$O(h^2)$

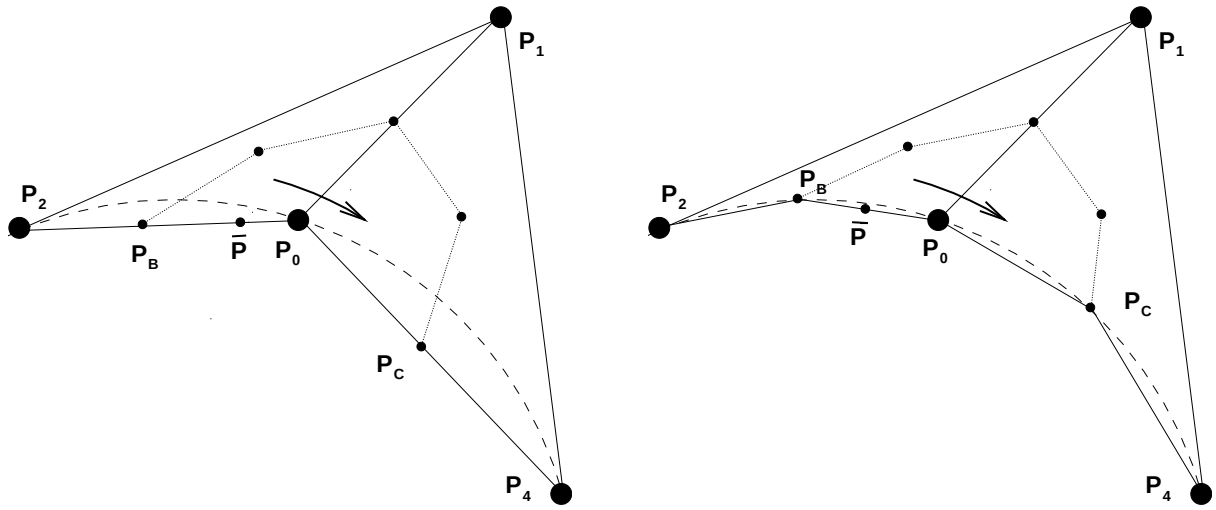

(a) Basic median-dual approximation for the edge-reconstruction scheme

(b) Modified approximation for the linear face-reconstruction scheme

Figure 11: *Straight-segment approximations to curved tangency boundary.*

the edge-reconstruction scheme, discrete tangency is enforced over the straight segments $[P_0, P_B]$ and $[P_0, P_C]$. The exact continuous solution satisfies the tangency condition at the actual curved boundary, not at the straight boundary segments. If evaluated with the exact solution, one boundary segment would appear as inflow, while the other would appear as outflow.

To assess the error introduced by implementing zero velocities over the straight boundary segments, consider the segment $[P_B, P_0]$ that contributes to the control volume centered at P_0. An overspecified version of the boundary conditions, in which the exact velocities are reconstructed at $\bar{P} = 5/6P_0 + 1/6P_2$, would complement the interior edge-reconstruction formulation to provide a 2^{nd}-order accurate solution. Thus, the difference between this overspecified boundary flux and the weak tangency boundary condition can be considered as a velocity reconstruction error. In particular, for the mass conservation law, the leading contribution to $R(Q)$ from the segment $[P_0, P_B]$ can be estimated as

$$R_{[P_B,P_0]} = \bar{\mathbf{V}} \cdot \bar{\mathbf{n}} = O(h), \tag{32}$$

where

$$\bar{\mathbf{V}} = \tfrac{5}{6}\mathbf{V}_0 + \tfrac{1}{6}\mathbf{V}_2 = \tfrac{1}{2}\left(\mathbf{V}_0 + \mathbf{V}_2\right) + O(h),$$
$$\bar{\mathbf{n}} = \tfrac{1}{2}\left(\hat{\mathbf{n}}_0 + \hat{\mathbf{n}}_2\right) + O(h^2).$$

and

$$\left(\mathbf{V}_0 + \mathbf{V}_2\right) \cdot \left(\hat{\mathbf{n}}_0 + \hat{\mathbf{n}}_2\right) = O(h^2),$$

Here, $\bar{\mathbf{V}}$ is the velocity vector reconstructed at $\bar{P}$ and $\bar{\mathbf{n}}$ is the outward unit normal corresponding to $[P_0, P_B]$, $\mathbf{V}_0$, $\hat{\mathbf{n}}_0$, $\mathbf{V}_2$, $\hat{\mathbf{n}}_2$, are the exact velocities and unit normals at the grid nodes P_0 and P_2, respectively, satisfying $(\mathbf{V}_0 \cdot \hat{\mathbf{n}}_0) = (\mathbf{V}_2 \cdot \hat{\mathbf{n}}_2) = 0$, and h is the characteristic meshsize. The 1^{st}-order accuracy in $R(Q)$ leads to local 1^{st}-order accurate discretization errors. The reason for the residual contribution, $R_{[P_B,P_0]}$, to be $O(h)$ is the 1^{st}-order difference between $\bar{\mathbf{V}}$ and $(\mathbf{V}_0 + \mathbf{V}_2)/2$. Similar $O(h)$ contributions appear in momentum-conservation equations.

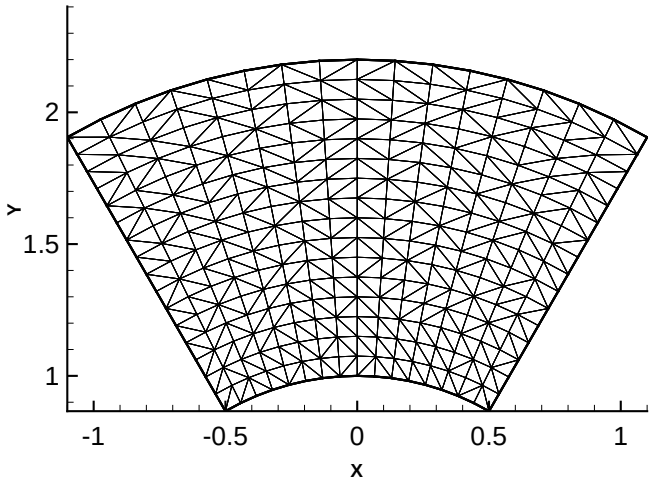

Figure 12: *Random triangular grid around the top of the cylinder.*

To illustrate the effect of a straight-segment approximation to a curved tangency boundary, a sequence of random triangular grids is generated at the top of the cylinder ($1 \le r \le 2.2$, $\pi/3 \le \theta \le 2\pi/3$) and used in computations with the edge-reconstruction FVD scheme; a grid example is shown in Figure 12. Figure 13 illustrates convergence of the L_1 norm of truncation and discretization errors in grid-refinement and DS tests performed with edge-reconstruction FVD scheme. Two DS tests are performed, each with the focal point at the top surface of the cylinder. The first DS test uses overspecification at all boundaries except the interior tangency nodes.

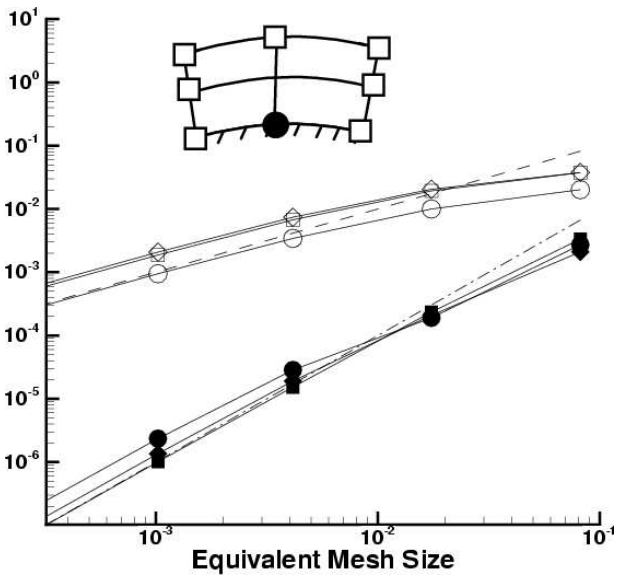

(a) DS test: interior tangency boundary conditions

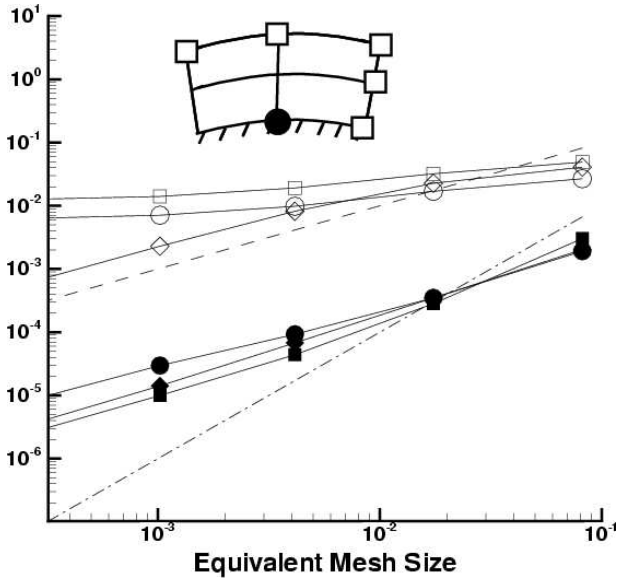

(b) DS test: inflow/tangency boundary conditions

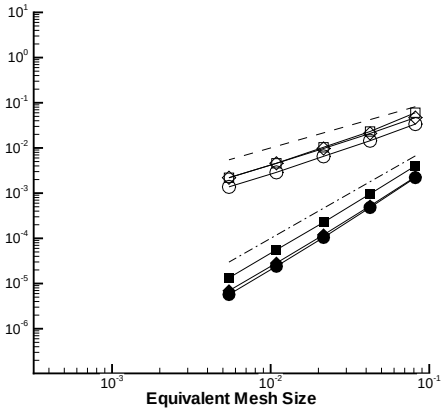

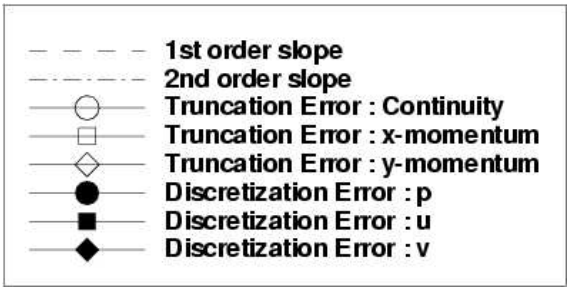

(c) Grid refinement

Figure 13: *Convergence of the L_1 norm of truncation and discretization errors observed in DS and grid-refinement tests for the edge-reconstruction FVD scheme. The tests are performed on randomly-split triangular grids at the top of the unit cylinder. The open square symbols in the sketches denote overspecified interface nodes for the DS tests.*

The second DS test replaces the overspecification along one boundary with the physical inflow boundary condition (see sketches in Figure 13).

For the interior-tangency nodes, there are two tangency segments; the errors at these segments

contribute to $R(Q)$ with opposite signs and, at least partially, compensate each other. Because of this compensation, the accuracy deterioration does not affect interior-tangency nodes on the grids with (nearly) uniform boundary node distributions. The 2^{nd}-order convergence of discretization errors and the 1^{st}-order convergence of truncation errors demonstrated in the interior-tangency DS test confirm this conclusion. However, in the corners or/and at the interfaces between clusters of boundary nodes with different topology/spacing, the compensation does not occur. The accuracy deterioration is clearly observed in the DS test performed with the inflow/tangency boundary conditions. The convergence of the L_1 norms of the errors in the grid-refinement test is the same as convergence shown in the interior-tangency DS test and is not affected by local accuracy deterioration in the corners; although not shown, the grid-refinement convergence of the L_∞ norm of errors is similar to the convergence demonstrated in the DS test with the inflow/tangency boundary conditions. A similar accuracy deterioration can occur on mixed-element grids at non-smooth interfaces between clusters of triangles and quadrilaterals; examples are shown in Appendix C.

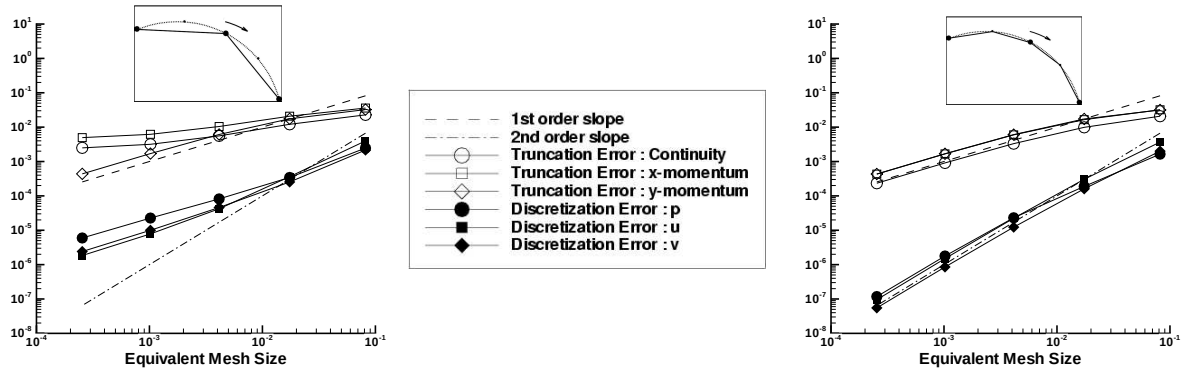

(a) DS test: basic approximation

(c) DS test: modified approximation

Figure 14: *Convergence of the L_1 norm of truncation and discretization errors observed in DS tests for the linear face-reconstruction FVD scheme with two types of straight-segment approximation to the curved tangency boundary.*

The linear face-reconstruction scheme possesses the flexibility to recover the 2^{nd}-order accuracy with a straight-segment tangency boundary approximation. Two required modifications are illustrated in the sketch (b) of Figure 11: (1) the points P_B and P_C are moved to the boundary, and (2) the fluxes are reconstructed at the midpoints of the straight boundary segments, e.g., at $\bar{P} = 1/2P_B + 1/2P_0$. Figure 14 shows convergence of the L_1 norm of truncation and discretization errors observed in DS tests for the linear face-reconstruction FVD scheme with two types of straight-segment approximation to the curved tangency boundary: the basic median-dual approximation and the modified approximation. The tests are performed in the setting similar to the inflow/tangency boundary conditions used with the edge-reconstruction scheme. The results confirm that, with modifications (1) and (2), the 2^{nd}-order convergence can be achieved with linear polynomials and a straight-segment approximation to the curved tangency boundary. Slower convergence observed with the basic median-dual cells indicates that both modifications are essential. Although not shown, with the quadratic face-reconstruction scheme and a quadratic fit to the curved tangency boundary, discretization errors converge with the 3^{rd} order.

5.3 Discretization error deterioration at stagnation

Local discretization accuracy deterioration may occur in the vicinity of stagnation or near other singularities in degenerated equations. To explain this phenomenon, we consider a one-dimensional symmetry-line nonlinear convection equation

$$uu_x = f \tag{33}$$

linearized around the leading-edge stagnation solution for the flat-plate geometry ($u = -x$)

$$-x\partial_x^h \delta^u - \delta^u = g, \quad \delta^u(-1) = \delta_{\text{inflow}}, \tag{34}$$

where ∂_x^h is a discrete derivative approximation; the same equation describes the tangency flow in the vicinity of the trailing-edge stagnation. The solution of (34) represents the discretization error, δ^u. The right-hand side g is $O(h^p)$ small for p^{th}-order discretizations and represents possible residual perturbations; the inflow condition, $\delta^u = 0$ defined at $x = -1$, may also contain an $\delta_{\text{inflow}} = O(h^p)$ error. The general solution of the initial-value problem (13) on the interval $x \in [0,\, 1]$ is given by

$$\delta^u = \delta^u_{\text{specific}}(x) \; + \; \frac{\delta^u_{\text{specific}}(-1) - \delta_{\text{inflow}}}{x}, \tag{35}$$

where $\delta^u_{\text{specific}}(x)$ is a specific solution of the equation (34). The function $\delta^u_{\text{specific}}(x)$ and the constant δ_{inflow} are both $O(h^p)$ small. However, the discretization error δ^u grows as $O(1/x)$ in the vicinity of stagnation ($x = 0$) and locally becomes $O(h^{p-1})$.

Analysis of the equivalent linear operator performed for the inviscid equations is also capable of detecting the discretization-error deterioration. In the vicinity of stagnation, both velocity components become $O(h)$ small and the equivalent operator becomes

$$E(Q) = \begin{pmatrix} O(1) & O(1) & 0 \\ O(h) & O(h) & O(1) \\ O(h) & O(h) & O(1) \end{pmatrix}, \tag{36}$$

cf. (28). Thus,

$$J^{-1}(Q) \sim E^{-1}(Q) = O\left(h^{-1}\right) \begin{pmatrix} O(h) & O(1) & O(1) \\ O(h) & O(1) & O(1) \\ O(h^2) & O(h) & O(h) \end{pmatrix}. \tag{37}$$

For the velocity discretization errors, the asymptotic order of $J^{-1}(Q)$ becomes $m_J = -1$, but for the discretization error in pressure, the asymptotic order remains the same as in the interior, $m_J = 0$, implying different orders of convergence for different variables at stagnation. To retain uniformly the same discretization-error convergence for all variables, one has to approximate the momentum conservation equations at stagnation with higher order than in the interior. Another curious observation is that the mass conservation law can be approximated with a lower accuracy order without inflicting discretization-error deterioration.

Discretization accuracy deterioration in the vicinity of stagnation is a universal phenomenon and expected for any discretization of the inviscid flow equations. In simulations, the stagnation accuracy deterioration is rarely noticed and seldom correctly attributed because its effect is mostly

visible far downstream of stagnation. At stagnation, the solution and all its derivatives are very small; therefore, in spite of increased relative discretization error, the absolute value of the local error, which is proportional to some derivative of the solution, does not exceed a typical error away from stagnation. Also, the effect disappears in the presence of the diffusion terms that prevent equation degeneration at stagnation. The discretization error generated at stagnation tends to be amplified by accelerated flow convecting the error downstream. For leading-edge stagnation, this stagnation-generated error is convected downstream along the tangency boundary, affects very few points, and is almost not observable in integral norms, such as L_1 and L_2 norms, but can be clearly detected in the L_∞ norm. At the trailing-edge stagnation, the generated discretization error is convected into the interior affecting more points. This may explain the difficulties observed in solution of the trailing edge flow problems, even for relatively benign geometries such as flat-plate, cylinder, or parabola.

In order to see the loss of accuracy more clearly, the DS test at stagnation needs to be adjusted to evaluate the relative discretization error, defined as $|E_d| \,/\, |Q|$, where, for computing the relative discretization error in the velocities, $|Q|_{vel} = \max\left(\sqrt{u^2+v^2}\right)$ and, for the relative discretization error in the pressure, $|Q|_p = \max(p)$. At stagnation, $|Q|_{vel} = O(h)$ and $|Q|_p = O(1)$.

Table 4: *Convergence of discretization and truncation errors for various unstructured grid formulations of the 2D inviscid incompressible equations at the aft of the unit cylinder. A single entry of α in the table indicates it refers to all the variables (u, v, p).*

Formulation	Error convergence at trailing-edge stagnation, $O\left(h^\alpha\right)$				
	DS test		Grid-refinement computations		
	Relative Discr. Error	Trunc. Error	Discr. Error		Trunc. Error
			L_1 norm	L_∞ norm	
Edge-reconstruction, randomly-split triangular grid	$u, v : \alpha = 1$ $p : \alpha = 2$	$\alpha = 1$	$1 < \alpha < 2$	$\alpha = 1$	$\alpha = 1$
Edge-reconstruction, random mixed-element grid	$u, v : \alpha = 0$ $p : \alpha = 1$	$\alpha = 0$	$0 < \alpha < 1$	$\alpha = 0$	$\alpha = 0$
Linear face-reconstruction, random mixed-element grid	$u, v : \alpha = 1$ $p : \alpha = 2$	$\alpha = 1$	$1 < \alpha < 2$	$u, v : \alpha = 1$ $p : 1 < \alpha < 2$	$\alpha = 1$
Quadratic face-reconstruction, random mixed-element grid	$u, v : \alpha = 2$ $p : \alpha = 3$	$\alpha = 2$	$2 < \alpha < 3$	$\alpha = 2$	$\alpha = 2$

Table 4 summarizes the error convergence orders observed in computations at the aft of the unit cylinder. Each global grid is formed from an underlying structured quadrilateral grid spanning 120 degrees in θ (centered about the most downstream point on the cylinder surface) with extent $1 \leq r \leq 2.2$ in the radial direction; the grids are generated with $2^{n+3} + 1$ points in both the radial and circumferential directions, where $n = 0,\ 1,\ 2,\ 3,\ 4$. The structured quadrilaterals are split randomly into a fully-triangular grid or a mixed-element grid, as discussed previously. The DS test is generated by grid-scaling the coarsest grid with the focal point at the most downstream point on the cylinder. The DS test is sharp in predicting convergence order of truncation errors and the L_∞ norm of discretization errors in the grid-refinement computations. The integral L_1 norm of the discretization error is less sensitive because the locally increased relative discretization

error in velocities has the strongest influence on the solution along the streamline coming from the stagnation; areas away from this streamline are affected much less. Note also that a clear distinction between convergence of relative discretization errors in the velocities and pressure predicted by (37) is observed only in the DS tests; in the global grid refinement computations, the nonlinear interactions slow the convergence of discretization error in pressure, although, the pressure errors remain much smaller than the velocity discretization errors on the same grids.

6 DISCUSSION

A new computational analysis tool, downscaling (DS) test, has been introduced and applied for studying the convergence rates of truncation and discretization errors for general unstructured-grid finite-volume discretization (FVD) schemes. The study corrects a misconception that the discretization accuracy of FVD methods on irregular grids is directly linked to convergence of truncation errors. The DS test is a general, efficient, accurate and practical tool, enabling straightforward verification and validation of general unstructured-grid formulations. It also allows separate analysis of the interior, boundaries, and singularities that could be useful even in structured-grid settings.

There are several new findings arising from the use of the DS-test analysis. It was shown that the discretization accuracy of a common node-centered edge-reconstruction FVD scheme, known to be 2^{nd}-order accurate for inviscid equations on triangular grids, degenerates to 1^{st} order for mixed grids. Alternative node-centered face-reconstruction schemes have been presented and demonstrated to provide 2^{nd} and 3^{rd} order accuracies on mixed grids. Appendixes B and C report on generation and propagation of discretization errors at typical interfaces between triangular and quadrilateral cells. A method improving the discretization accuracy at general non-smooth mixed-element interfaces has been suggested. The local accuracy deterioration at intersections of tangency and inflow/outflow boundaries has been demonstrated using DS tests tailored to examine the local behavior of the boundary conditions. The discretization-error order reduction within inviscid stagnation regions has been demonstrated. The accuracy deterioration is local, affecting mainly the velocity components, but applies to any order scheme. The result is somewhat surprising because the solution is so simple but analysis of the Jacobian operator along the stagnation streamline has provided insight into the phenomena.

In 2-D inviscid computations, the cost of computing residuals of the face-reconstruction discretizations is about twice as large as the cost of edge-reconstruction residuals because the face-reconstruction discretizations require a solution of the approximate Riemann problem at each control-volume segment (face); the edge-reconstruction discretization requires one Riemann solution per two connecting segments. The cost increase in 3D computations for general tetrahedral grids is much larger because multiple dual control-volume faces are adjacent to each primal-mesh edge. As a possible dramatic cost reduction, one can evaluate the dissipation at the midpoints of primal-mesh edges, in the same way as in the edge-reconstruction discretization, once for all adjacent dual segments/faces, while unsplit flux contributions are evaluated at the dual segments/faces. Also, as shown in Appendix A, the cost of face-reconstruction FVD schemes on cell-centered grids is much lower.

On typical 2-D unstructured grids, where most nodes have at least five neighbors, a typical computational stencil for the quadratic face-reconstruction discretization has the same size as a stencil for the linear face-reconstruction scheme. The memory requirements for the quadratic discretization are about two times higher than for linear discretizations because a larger number of coefficients is stored at each control volume.

A CONTROL SURFACE COMPLEXITY IN THREE DIMENSIONS

The complexity associated with flux integration in three-dimensional cell-centered or node-centered FVD schemes is estimated. The complexity is measured as the number of flux-reconstruction instances required for one residual evaluation. Flux reconstructions are the main contributers to the operation counts associated with flux integration; other aspects of the discretization, such as determining the solution values or solution-gradient values require additional considerations. Three types of primal meshes are considered: (1) fully-tetrahedral, (2) fully-prismatic, (3) fully-hexahedral.

An underlying Cartesian grid is considered and split into the various elements. The splitting into tetrahedra assumes each hexahedral defined by the grid is split into 5 tetrahedra with one of the tetrahedra being completely interior to the hexahedral (i.e., its faces are not aligned with any of the hexahedral faces – see Figure 15). Only interior discretizations are estimated; boundary effects are neglected.

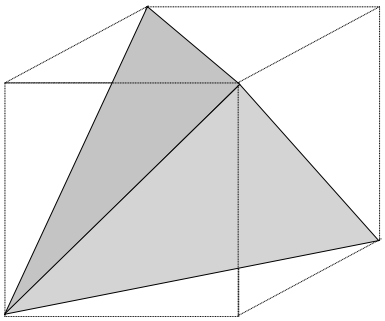

Figure 15: *Splitting hexahedral into 5 tetrahedra*

Table 5: *Number of flux-reconstruction instances per equation for 3D FVD discretizations.*

Elements	Cell-centered face-reconstruction	Node-centered edge-reconstruction	Node-centered face-reconstruction
Tetrahedral	4 (4)	12	120 (60)
Prismatic	8 (5)	8	72 (36)
Hexahedral	12 (6)	6	48 (24)

Table 5 shows complexity estimates for two node-centered and one cell-centered 3D FVD schemes. Both node-centered discretizations assume a median-dual partition of the domain. In such a partition, the constituent dual control volumes are bounded by generally non-planar dual faces formed by connecting 3 types of points: (1) edge midpoints, (2) element-face centroids, and (3) element centroids. The edge-reconstruction FVD scheme approximates integration over all of the constituent dual faces surrounding an edge midpoint by evaluating flux at the edge midpoint with directed area taken as the combined directed area. The face-reconstruction schemes reconstruct fluxes at each of the constituent dual faces separately with local directed areas. For the present estimation, we assume that each flux-reconstruction instance requires the same operation count, in particular, the approximate Riemann solver is applied at each reconstruction point.

As mentioned previously, significant saving can be achieved, if the dissipation matrix is computed once for all control surfaces surrounding an edge. The first node-centered scheme is a 3D version of the edge-reconstruction FVD scheme discussed in Section 5.2.2; the second node-centered scheme is an extension of the 2D linear face-reconstruction FVD scheme introduced in Section 5.2.3. The cell-centered formulation uses integration scheme with one flux reconstruction per control face.

Two estimates of complexity are given. The first estimate assumes that any constituent quadrilateral face in the control surface is broken into two triangular faces. The second estimate (in parentheses) assumes any constituent quadrilateral face is approximated as planar. The former is required to ensure a precise (water-tight) definition of the control surface and can serve as a measure of the complexity in integration of the physical flux terms. The latter can serve as an estimate of the complexity associated with numerical dissipation terms, in which details of the control-surface can be neglected.

The complexities of cell-centered and edge-reconstruction node-centered FVD schemes are reasonably close. Unfortunately, as shown in this paper, the accuracy of the edge-reconstruction FVD scheme degenerates to 1^{st} order on general mixed-element grids. To maintain the 2^{nd}-order accuracy on general grids, one can employ the face-reconstruction node-centered scheme, but the integration complexity of this formulation substantially exceeds the complexity of the cell-centered FVD scheme. These results are in agreement with the observations made by Delanaye and Liu [6], which led them to selection of a cell-centered discretization.

B INTEGRATION ACCURACY OF EDGE-RECONSTRUCTION SCHEME ON MIXED GRIDS

It was shown earlier [2, 3, 4] that the edge-reconstruction scheme provides exact integration of linear fluxes on general triangular grids because of one-to-one correspondence with a 2^{nd}-order accurate finite-element formulation. Examples in this section illustrate deterioration of the integration accuracy to 1^{st} order on general mixed-element grids as well as on quadrilateral grids consisting of irregular cells. In this section, quadrilateral cells are referenced as regular if they approach a rectangular shape in the limit of grid refinement. A 2^{nd}-order integration scheme is expected to provide exact integration over a control volume boundary for arbitrary linear fluxes; any deviation from the exact value indicates accuracy deterioration. For illustration, we assume a linear flux $\mathbf{F} = (U, V)^T = (y, 0)^T$ and the central vertex 0 to be located at the origin $(x, y) = (0, 0)$.

The first example illustrates accuracy deterioration on general mixed-element grids. Figure 16 shows a grid composed of five cells, one square and four right triangles, and the corresponding median-dual control volume with boundary Γ; all vertexes are located on a uniform Cartesian mesh with meshsize $h = 1$.

The exact value of the contour integral is

$$\oint_{\Gamma} (\mathbf{F} \cdot \hat{\mathbf{n}}) \, d\Gamma = 0, \tag{38}$$

where $\hat{\mathbf{n}}$ is the outward unit normal. With the edge-reconstruction scheme, the flux is evaluated at the edge midpoints with the vertical coordinates $y_{[01]} = y_{[04]} = 0, y_{[02]} = y_{[03]} = 0.5, y_{[06]} = -0.5$. The discrete contour integral is computed as

$$-y_{[02]}\frac{1}{3} + y_{[03]}\frac{1}{3} - y_{[06]}\frac{1}{6} = \frac{1}{12}, \tag{39}$$

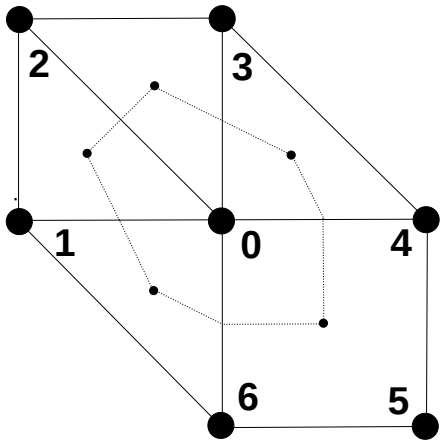

Figure 16: *Illustration for edge-reconstruction flux integration scheme on mixed grids.*

which differs from the exact value. The face-reconstruction schemes recover the exact value of the contour integral.

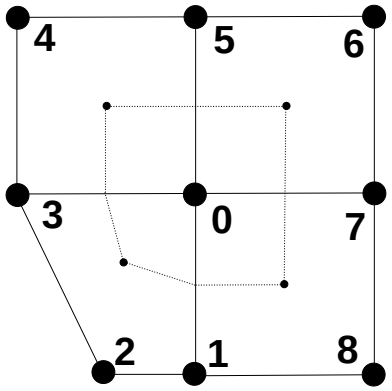

Figure 17: *Illustration for edge-reconstruction flux integration scheme on perturbed quadrilateral grids.*

The second example shows accuracy deterioration on a quadrilateral grid containing irregular cells. Figure 17 illustrates a quadrilateral grid with three squares and one trapezoid. All vertexes, beside vertex 2, are located on a uniform Cartesian grid with meshsize $h = 1$. The short basis of the trapezoid 0123 is two times shorter than the long one; the centroid of the trapezoid is located at $(x, y) = (-7/18, -4/9)$. The exact value of the contour integral is again zero; the approximation provided by the edge-reconstruction scheme is $1/36$. The face-reconstruction schemes recover the exact value of the contour integral. Note that one common version of the edge-reconstruction scheme, which uses the arithmetic average of the vertexes instead of the centroid as the primal-cell

center, provides the exact answer for integration of the flux $\mathbf{F} = (y, 0)^T$ for the geometry shown in Figure 17, but deviates from the exact integration for $\mathbf{F} = (x, 0)^T$ on the same grid.

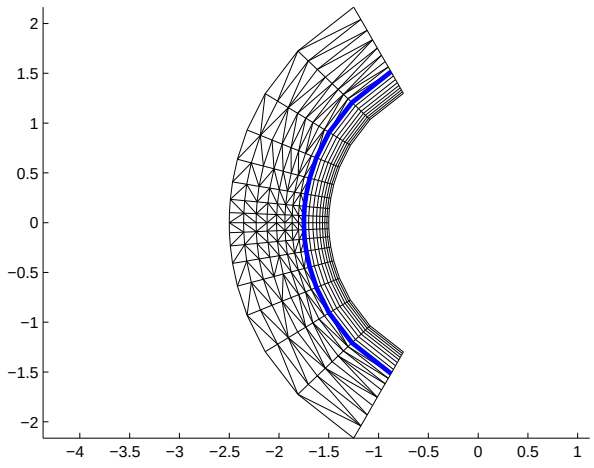

Figure 18: *Example of a mixed-element grid with smooth interface.*

The examples above show that the edge-reconstruction scheme provides 1^{st}-order integration accuracy on general unstructured grids; nevertheless, there are important practical cases where 2^{nd}-order accuracy can be recovered. For example, the edge-reconstruction scheme provides 2^{nd}-order integration accuracy on mixed-element grids that have clusters of general triangular cells, mapped clusters of quadrilateral cells, and a smooth interface separating these clusters of primal cells. Mapped clusters of quadrilateral cells are derived from uniform (possibly anisotropic) Cartesian grids by smooth mapping. An example of a mapped cluster is a stretched bodyfitted (sub-)grid with a stretching factor (i.e., the ratio of adjacent meshsizes) $\beta = 1 + O(h)$, where h is a characteristic distance across cells used in verification of the consistent refinement property. An interface is considered smooth if the unit normal changes smoothly with the distance along the line separating clusters of triangular and quadrilateral cells. An example of a mixed-element grid with a smooth interface is shown in Figure 18; the bold line highlights the interface separating a mapped cluster of regular quadrilaterals and a cluster of randomly-split triangles.

To provide insight into recovering the 2^{nd}-order accuracy on grids with smooth interfaces, we consider a grid consisting of four cells, two triangular and two rectangular, separated by a straight-line interface; the grid and the corresponding dual control volume with the boundary Γ are shown in Figure 19. The integral over the contour $\oint_{\Gamma}$ can be split into two contour integrals, $\oint_{ABCP_0GH}$ and $\oint_{CDEFGP_0}$. Our goal is to show that there is an approximation to the integral over the interface $\int_{GP_0C}$ that makes both normalized integrals, $\frac{1}{|\Gamma|}\oint_{ABCP_0GH}$ and $\frac{1}{|\Gamma|}\oint_{CDEFGP_0}$, 2^{nd}-order accurate. Approximations to integrals over other segments are computed according to the edge-reconstruction scheme.

The following derivation relies on the fact that the edge-reconstruction scheme provides the 2^{nd}-order integration accuracy on general triangular grids and on regular quadrilateral grids assuming proper boundary closures, e.g., the boundary closures discussed in Section 5.2.2. Let us

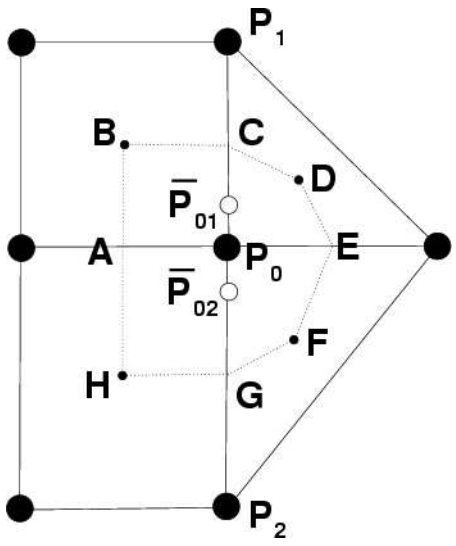

Figure 19: *Illustration of a mixed-element grid with a smooth interface separting general triangles and regular quadrilaterals*

treat the interface between the triangular and rectangular cells as a boundary of the cluster of triangular cells. This approach ensures 2^{nd}-order accuracy in approximating $\frac{1}{|\Gamma|}\oint\limits_{CDEFGP_0} F(P)$, where $F(P)$ is an arbitrary (piecewise smooth) function. Thus, the approximation to the interface integral is computed as

$$\int\limits_{GP_0C} F(P) = \frac{1}{2}\left[F(\bar{P}_{01})|P_0,P_1| + F(\bar{P}_{02})|P_0,P_2|\right], \tag{40}$$

where $\bar{P}_{01} = 5/6P_0 + 1/6P_1$ and $\bar{P}_{02} = 5/6P_0 + 1/6P_2$. To establish the 2^{nd}-order accuracy for $\frac{1}{|\Gamma|}\oint\limits_{ABCP_0GH}$, we need to satisfy the following relation

$$\frac{1}{|P_1,P_2|}\left(F(\bar{P}_{01})|P_0,P_1| + F(\bar{P}_{02})|P_0,P_2|\right) = F(P_0) + O(h^2). \tag{41}$$

Indeed, using the Taylor expansion,

$$\frac{F(\bar{P}_{01})|P_0,P_1| + F(\bar{P}_{02})|P_0,P_2|}{|P_1,P_2|} = F(P_0) + F'(P_0)\left(|P_0,P_1| - |P_0,P_2|\right) + O(h^3), \tag{42}$$

where $F'(P_0)$ is the derivative of the function $F(P)$ along the interface. For mapped grids, $|P_0,P_1| - |P_0,P_2| = O(h^2)$.

The 2^{nd}-order integration accuracy can also be recovered on general mixed-element grids with irregular quadrilaterals and non-smooth interfaces if a 2^{nd}-order accurate face-reconstruction scheme is employed for nodes surrounded only by quadrilateral cells, the edge-reconstruction scheme is employed for nodes surrounded only by triangular cells, and a special conservative interface scheme is derived for other nodes. One possible methodology for derivation of the interface scheme requires introduction of auxiliary (hanging) nodes at the centers of edges (faces in 3D) separating triangles and quadrilaterals; these nodes are used to divide triangles attached to

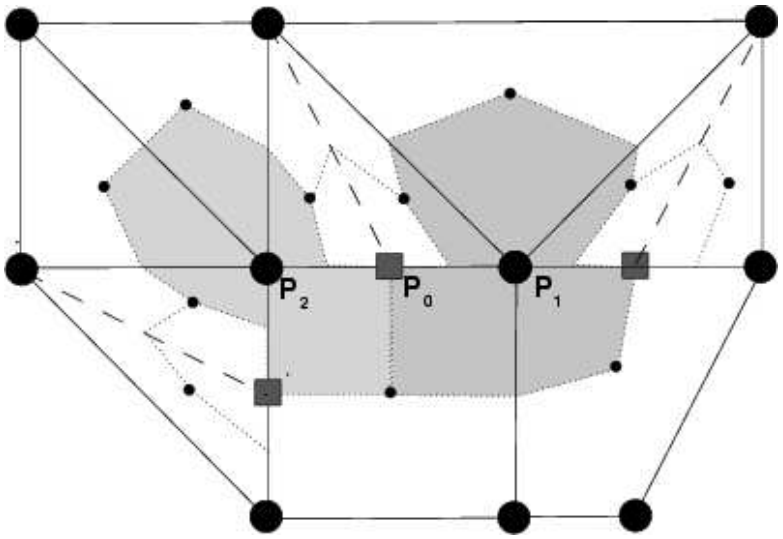

Figure 20: *Illustration of the interface scheme for transition between face-reconstruction scheme on quadrilaterals and edge-reconstruction scheme on triangles.*

the interface (see Figure 20). The control volumes around original nodes located at the interface are constructed by uniting corresponding dual volumes from triangular and quadrilateral domains (shaded volumes in Figure 20); volumes around auxiliary nodes are those from the triangular part only.

For flux integration, the interface is treated as a boundary for the triangular part of the domain, employing the integration techniques explained in Section 5.2.2. In particular, for integration of the interface segments of the control-volume boundaries, the solution is reconstructed at the point $\bar{P} = 5/6P_0 + 1/6P_1$, where P_0 and P_1 are the neighboring grid nodes located at the interface (see Figure 20); for integration over the control-volume boundary segments attached to the interface from the triangular side, the solution is reconstructed at the attachment point. All integrations over control-volume boundary segments located within quadrilateral cells are performed according to a 2^{nd}-order accurate face-reconstruction scheme. Note that on mixed-element grids, which include quadrilateral cells only within clusters of mapped quadrilaterals, edge-reconstruction scheme can also be used for nodes surrounded by quadrilaterals.

C EDGE-RECONSTRUCTION SCHEME: CONVERGENCE OF DISCRETIZATION ERRORS ON MIXED-ELEMENT GRIDS WITH NON-SMOOTH INTERFACES

In this appendix, we consider convergence of truncation and discretization errors of the edge-reconstruction scheme for the conservation laws with fluxes (26) on mixed-element grids with clusters of triangular and rectangular cells. As a result of integration accuracy degradation, discretization errors of 1^{st} order are generated at non-smooth interfaces between triangular and rectangular cells; thus, the L_∞ norms of truncation and discretization errors are expected to converge with the zeroth and first orders, respectively. In many cases, the generated discretization errors remain local, and integral (e.g., L_1 or L_2) norms of discretization errors converge faster than 1^{st} order. In problems with strong convection, however, the generated discretization errors can translate downstream contaminating large portions of the computational domain and leading to a 1^{st}-order discretization-error convergence in all norms.

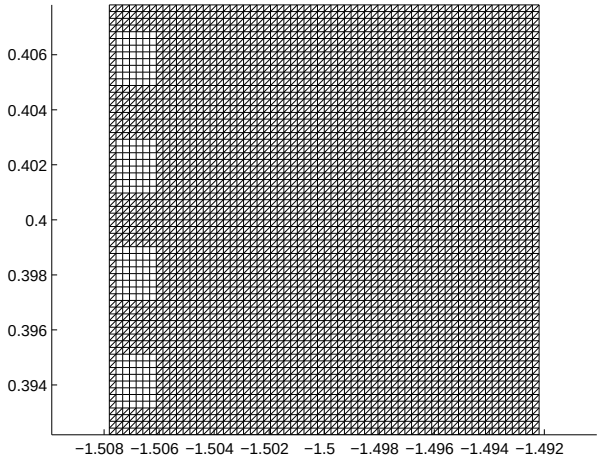

Figure 21: *A representative* 65×65*-node mixed-element grid with a non-smooth interface between triangular and rectangular cells*

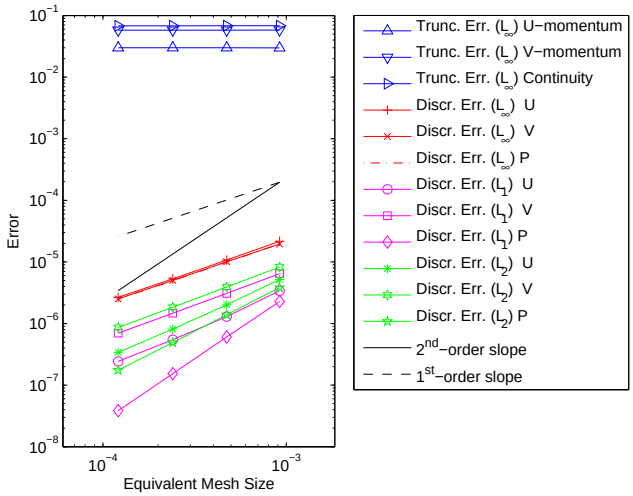

Figure 22: *Convergence history for computations on grids with a non-smooth interface between triangular and rectangular cells*

To illustrate generation and propagation of discretization errors, we consider a square domain with the side length of $1/64$ centered at $(x, y) = (-1.5, 0.4)$. The exact solution is the cylinder-flow solution (31). The discretization grids are derived from regular triangular grids. The vertical column, 6 meshsize wide, located one cell away from the inflow vertical boundary is divided into 6×8 rectangles; the triangular cells in each other rectangle are replaced with rectangular cells. A 65×65-node grid is shown in Figure 21. Edge-reconstruction scheme is applied. The convergence history of the L_∞ norms of truncation and discretization errors as well as L_1 and L_2

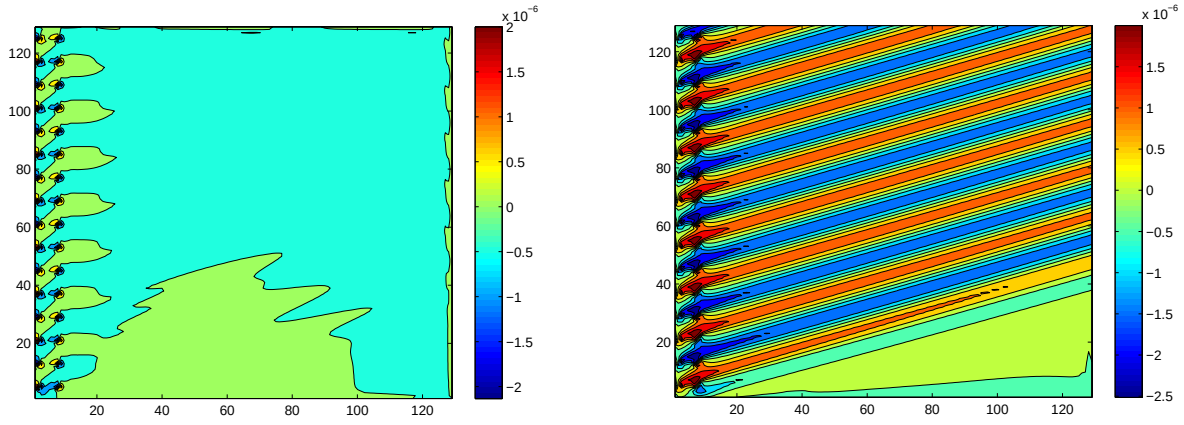

(a) Pressure, P

(b) Horizontal velocity, U

Figure 23: *Discretization error profile on* 129×129*-node mixed-element grid with a non-smooth interface between triangular and quadrilateral cells*

norms of discretization errors is shown in Figure 22. As expected, the L_∞ norms of truncation and discretization errors converge with zeroth and first order, respectively. Convergence of integral norms of discretization errors varies for different variables: the discretization errors in the velocity components, U and V, exhibit a 1^{st}-order convergence; the L_2 norms of the discretization errors in the pressure, P, converge faster than 1^{st} order, but slower than 2^{nd} order; convergence of the L_1 norms for the pressure errors is 2^{nd} order. A detailed profile of discretization errors in U and P shown in Figure 23 explains the observed variation in convergence rates. For all variables, 1^{st}-order discretization errors are generated at the corners where rectangular cells are surrounded by triangles; however, the generated pressure errors remain local, while the errors in U propagate downstream.

The sequence of mixed-element grids used in this example has been tuned to demonstrate 1^{st}-order discretization-error convergence in all norms; however, in practical computations on general mixed-element grids, certain errors cancellations are quite common, and the integral norms of discretization errors exhibit convergence rates that are between 1^{st} and 2^{nd} order. The next example presents a mixed-element grid with substantial error cancellations.

Numerical tests with the same cylinder-flow solution (31) are performed on mixed-element grids with a diagonal interface that is non-smooth everywhere. A representative grid and discretization-error convergence history are shown in Figure 24. While not shown, the truncation errors converge with zeroth order in the L_∞ norm. Convergence of the L_∞ norms of discretization errors is 1^{st} order, as expected. Convergence of the L_2 norms of discretization errors approaches 2^{nd} order. Improved L_2-norm convergence is explained by oscillations observed in the discretization errors along the interface. The oscillations lead to error cancellations downstream of the interface. The horizontal-velocity error profile is shown in Figure 25.

Note that the convergence results shown in Figure 24 contradict [11], where zeroth order convergence for the L_∞ norms of discretization errors and half-order convergence for the L_2 norms of discretization errors have been reported for a central edge-reconstruction scheme applied to a

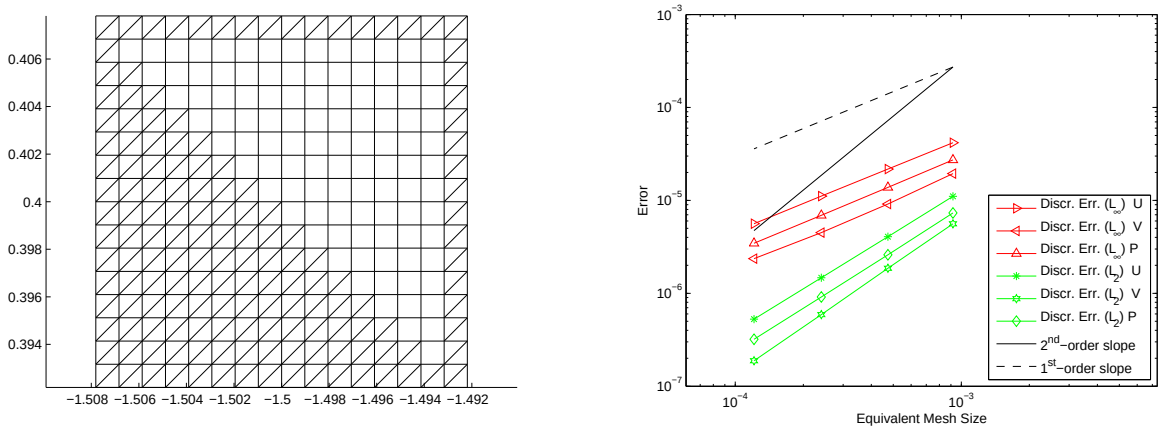

(a) Representative grid

(b) Convergence history

Figure 24: *A representative grid and convergence rates on mixed-element grids with a diagonal interface*

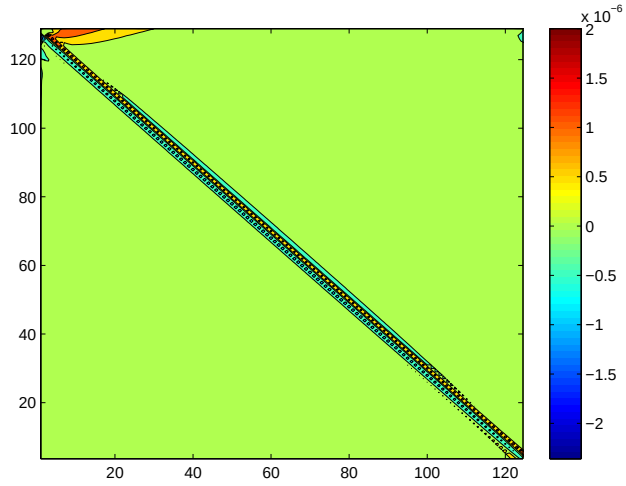

Figure 25: *Discretization error profile for the horizontal velocity component,* U*, on* 129×129*-node mixed-element grid with a diagonal interface*

constant-coefficient convection problem on a similar mixed-element grid. A possible explanation for this discrepancy is provided in Appendix D.

D EDGE-RECONSTRUCTION SCHEME ON PERTURBED QUADRILATERAL GRIDS

This section reports on investigation of the claim made in [11] that the edge-reconstruction scheme for perturbed quadrilaterals is zeroth order.

The considered uniform quadrilateral grids are Cartesian grids (Figure 26 (a)) defined on the domain $x \in [0, 1]$ and $y \in [0, 1]$. For the perturbed quadrilateral grids, all grid points are perturbed in both x and y directions by random shifts in the range $[-0.1, +0.1]$ of the local mesh size (Fig-

ure 26 (b)). The sequences of globally-refined grids are typically generated with $2^{n+3}+1$ points in both directions, where $n = 0,\ 1,\ 2,\ 3,\ 4,\ 5$.

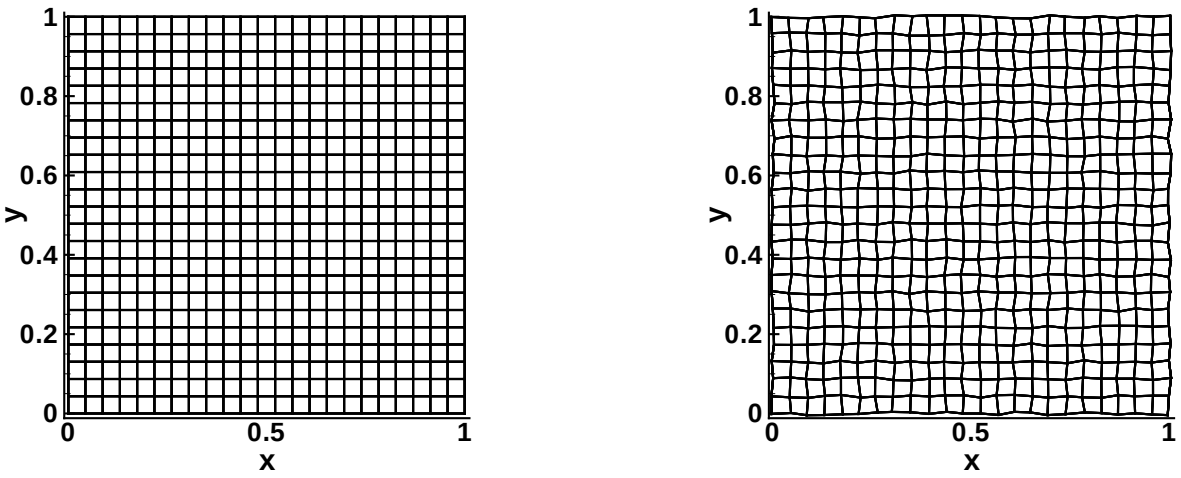

(a) Uniform grid.

(b) Perturbed grid.

Figure 26: *Typical computational grid (shown with 24 points in each direction of underlying Cartesian mesh).*

Following [11], the scalar convection equation is solved,

$$a\frac{\partial q}{\partial x} + b\frac{\partial q}{\partial y} = f, \tag{43}$$

where a and b are constants (taken as $a = b = 1$), q is the solution, and f is a forcing term. At the inflow boundary, q is specified from the solution. At the outflow boundary, the boundary flux is determined from the solution value at the nearest node point, referred to here as a weak closure condition. This closure is approximately a first-order upwind differencing closure and is also that advocated in [11].

The characteristic direction is defined as $\xi = (ax + by)/c$ where $c^2 = a^2 + b^2$. The cross-characteristic direction is defined as $\eta = (-bx + ay)/c$. There are four exact solutions considered:

$$q_1 = \sin(4\pi c\xi); \qquad f_1 = 4\pi c^2 \cos(4\pi c\xi). \tag{44}$$

$$q_2 = c(\xi + \xi^2/2); \qquad f_2 = c^2(1 + \xi). \tag{45}$$

$$q_3 = 0; \qquad f_3 = 0. \tag{46}$$

$$q_4 = \sin(\pi c\eta); \qquad f_4 = 0. \tag{47}$$

The first two solutions have variation in the characteristic direction; the third solution is trivial; the fourth solution has variation in the cross-characteristic direction only.

The L_1 norms of truncation and discretization errors are shown versus an effective meshsize parameter, taken as the L_1 norm of the square root of the dual volume. In the figures, the shaded symbols denote truncation errors and the open symbols denote discretization errors; the errors of the third solution are not shown.

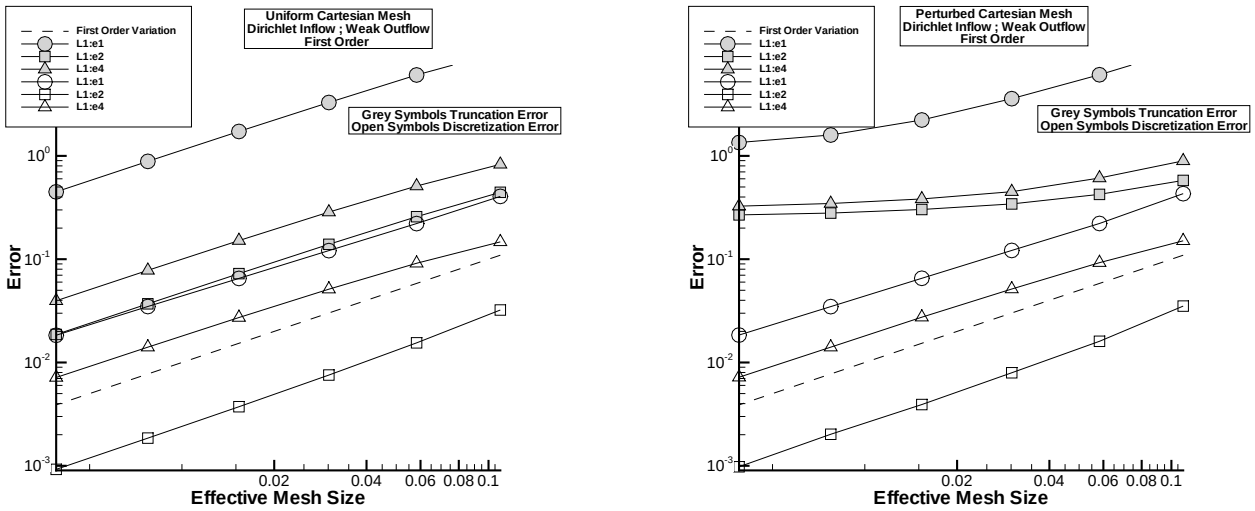

(a) Uniform grid.

(b) Perturbed grid.

Figure 27: *Errors in grid refinement for first-order upwind edge-reconstruction scheme.*

The results for the first-order accurate upwind edge-reconstruction scheme are shown in Figure 27. The results are consistent with analysis provided in this paper. For the uniform grids, both truncation errors and discretization errors show a first-order convergence. For the perturbed grids, the truncation errors show one-order reduction in convergence but the discretization errors remain first-order accurate. Variations of the magnitude of the discretization error norm between the uniform and perturbed grids with the same number of points are very small.

The results for the second-order accurate upwind-biased (Fromm-type) edge-reconstruction scheme are shown in Figure 28; this discretization uses the least-square gradient at a node to reconstruct the solution at the edge-midpoints. Again, the results are consistent with expectations. For the uniform grids, both truncation errors and discretization errors show a second-order convergence. For the perturbed grids, the truncation errors show no convergence, i.e., zeroth-order convergence. On coarse grids, the discretization error convergence is better than first order. For solutions q_2 and q_4, the discretization errors asymptote clearly to first-order accuracy on finer grids.

The results for the second-order accurate central edge-reconstruction scheme are shown in Figure 29; this discretization reconstructs the solution by averaging the two nodal values on either side of an edge. This scheme is susceptible to checkerboard instabilities and boundary conditions are prominent in eliminating unstable modes. For the uniform grids, both truncation errors and discretization errors show a second-order convergence. Although not shown, the discretization errors exhibit a checkerboard pattern over the mesh.

For the perturbed grids, the truncation errors show no convergence, although we do not show their variation. The variation of the discretization errors is shown for two grid sequences. The

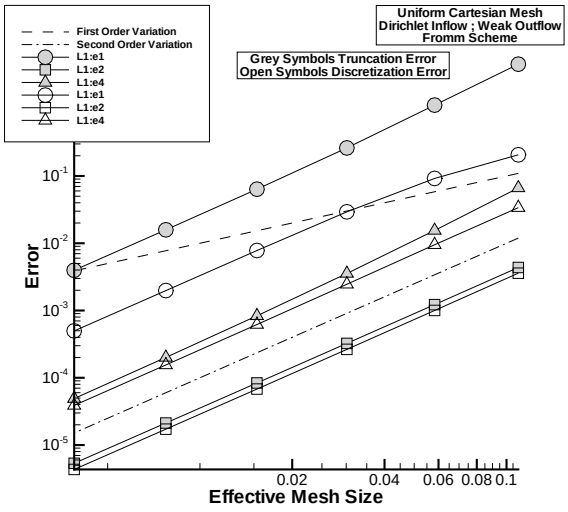

(a) Uniform grid.

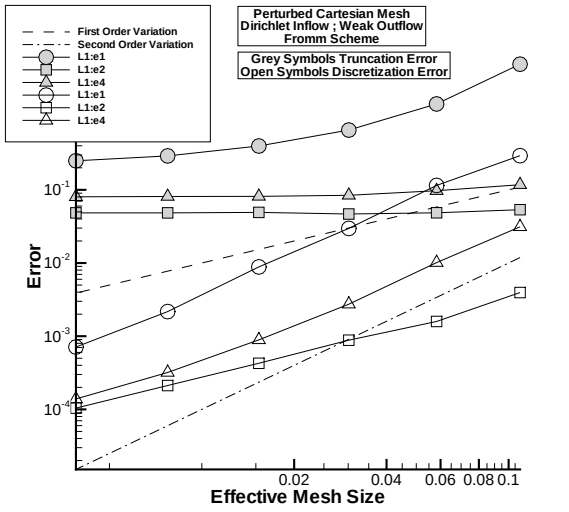

(b) Perturbed grid.

Figure 28: *Errors in grid refinement for second-order Fromm-type edge-reconstruction scheme.*

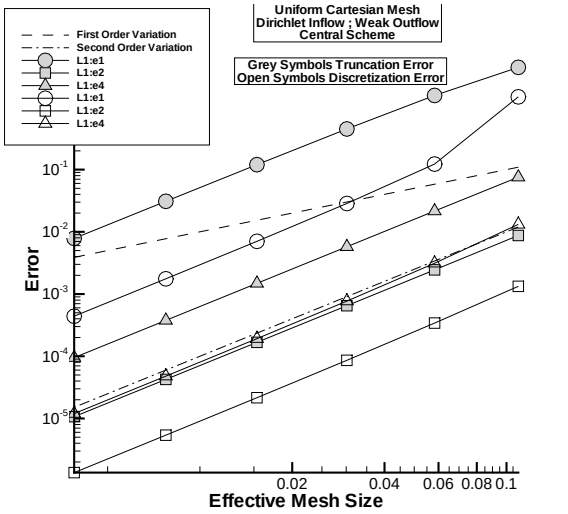

(a) Uniform grid.

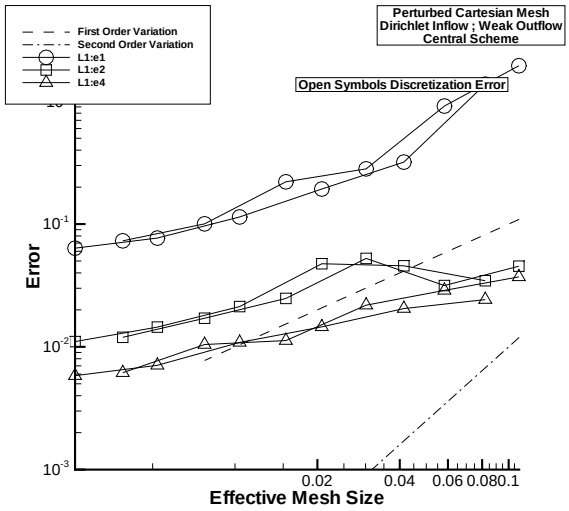

(b) Perturbed grid.

Figure 29: *Errors in grid refinement for second-order central edge-reconstruction scheme.*

discretization errors are quite erratic with grid refinement, as is typical of schemes with checkerboard instabilities. The discretization errors are converging but apparently at a rate slower than first-order. The only point to be made for this central scheme is that it appears to be convergent with grid refinement and not inconsistent as stated in [11].

Numerical results presented in this appendix show both the fully-upwind first-order edge-reconstruction scheme and an upwind-biased Fromm-type edge-reconstruction scheme to have first-order convergence of discretization errors on perturbed quadrilateral grids. These results are

consistent with the analysis and the results reported in the main body of this paper and in [1]. For the central edge-reconstruction scheme, the discretization errors are highly oscillatory spatially and the convergence of discretization error norms is highly erratic. The convergence of the discretization errors is apparently less than first order, but nonetheless the errors converge in all norms. The erratic behavior of the discretization errors may have led to an incorrect conclusion in [11]. Other discrepancies, such as zeroth order convergence of the L_∞ norms of the discretization errors and partial-order convergence of the L_2 norms of the discretization errors reported in [11] for computations on mixed grids are also attributed to the erratic convergence characteristic for schemes with checkerboard instabilities.

REFERENCES

[1] M. AFTOSMIS, D. GAITONDE, AND T. S. TAVARES, *Behavior of linear reconstruction techniques on unstructured meshes*, AIAA Journal, 33 (1995), pp. 2038–2049.

[2] W. K. ANDERSON AND D. L. BONHAUS, *An implicit upwind algorithm for computing turbulent flows on unstructured grids*, Computers and Fluids, 23 (1994), pp. 1–21.

[3] T. J. BARTH, *Numerical aspects of computing high-Reynolds number flow on unstructured meshes*, AIAA Paper 91-0721, 29-th AIAA Aerospace Science Meeting, Reno, NV, January 1991.

[4] ——, *Recent developments in high-order k-exact reconstruction on unstructured meshes*, AIAA Paper 93-0668, 31-st AIAA Aerospace Science Meeting, Reno, NV, January 1993.

[5] W. J. COIRIER, *An adaptively-refined, cartesian, cell-based scheme for the Euler and Navier-Stokes equations*, tech. rep., NASA TM-106754, October 1994.

[6] M. DELANAYE AND Y. LIU, *Quadratic reconstruction finite volume schemes on 3D arbitrary unstructured polyhedral grids*, AIAA Paper 1999-3259, 14-th AIAA CFD Conference, Norfolk, VA, June 1999.

[7] A. C. HASELBACHER, *A Grid-Tranparent Numerical Method for Compressible Viscous Flow on Mixed Unstructured Meshes*, PhD thesis, Loughborough University, 1999.

[8] A. C. HASELBACHER, J. J. MCGUIRK, AND G. J. PAGE, *Finite-volume discretization aspects for viscous flows on mixed unstructured grids*, AIAA Journal, 37 (1999), p. 477.

[9] M. HEMSCH AND J. MORRISON, *Statistical analysis of CFD solutions from the third AIAA drag prediction workshop*, AIAA Paper 2007-0254, 45-th AIAA Aerospace Science Meeting and Exhibit, Reno, NV, January 2007.

[10] L. KRIVODONOVA AND M. BERGER, *High-order accurate implementation of solid wall boundary conditions in curved geometries*, J. Comput. Phys., 211 (2006), pp. 492–512.

[11] MAGNUS SVÄRD AND JAN NORDSTRÖM, *An accuracy evaluation of unstructured node-centered finite-volume methods*, NIA Report 2005-04, NASA CR-2006-214293, April 2006.

[12] R. E. MINECK, J. L. THOMAS, AND B. DISKIN, *Analysis tools for CFD multigrid solvers*, AIAA Paper 2004-2532, 34-th AIAA CFD conference, Portland, OR, June 2004.

[13] K. W. MORTON AND T. SONAR, *Finite volume methods for hyperbolic conservation laws*, Acta Numerica, (2007), pp. 155–238.

[14] C. OLLIVIER-GOOCH, A. NEJAT, AND K. MICHALACK, *On obtaining high-order finite-volume solutions to the Euler equations on unstructured meshes*, AIAA Paper 2007-4194, 18-th AIAA CFD conference, Miami, FL, June 2007.

[15] P. J. ROACHE, *Verification and Validation in Computational Science and Engineering*, Hermosa, Albuquerque, NM, 1998.

[16] P. L. ROE, *Approximate Riemann solvers, parameter vectors, and difference schemes*, J. Comp. Phys., 43 (1981), pp. 357–372.

[17] ——, *Error estimates for cell-vertex solutions of the compressible Euler equations*, ICASE Report 87-6, NASA CR-1987-178235, January 1987.